Observing the Spatial and Temporal Evolution of Exciton Wave Functions in Organic Semiconductors

Marcel Theilen,[1,2] Siegfried Kaidisch,[3] Monja Stettner,[4,5,6] Sarah Zajusch,[1] Eric Fackelman,[4,5,6] Alexa Adamkiewicz,[1] Robert Wallauer,[1] Andreas Windischbacher,[3] Christian S. Kern,[3] Michael G. Ramsey,[3] François C. Bocquet,[4,5] Serguei Soubatch,[4,5] F. Stefan Tautz,[4,5,6,*] Ulrich Höfer,[1,2,†] and Peter Puschnig[3,‡]

[1]*Department of Physics, University of Marburg, 35032 Marburg, Germany*

[2]*Department of Physics and Regensburg Center for Ultrafast Nanoscopy (RUN), University of Regensburg, 93053 Regensburg, Germany*

[3]*Institute of Physics, University of Graz, 8010 Graz, Austria*

[4]*Peter Grünberg Institute (PGI-3), Forschungszentrum Jülich, 52425 Jülich, Germany*

[5]*Jülich Aachen Research Alliance, Fundamentals of Future Information Technology, 52425 Jülich, Germany*

[6]*Institut für Experimentalphysik IV A, RWTH Aachen University, 52074 Aachen, Germany*

(Received 2 December 2025; revised 30 June 2026; accepted 8 July 2026; published 28 August 2026)

Excitons, the correlated electron-hole pairs governing optical and transport properties in organic semiconductors, have long resisted direct experimental access to their full quantum-mechanical wave functions. Here, we use femtosecond time-resolved photoemission orbital tomography (trPOT) combining high-harmonic probe pulses with time- and momentum-resolved photoelectron spectroscopy to directly image the momentum-space distribution and ultrafast dynamics of excitons in α-sexithiophene thin films. We introduce a model that enables reconstruction of the exciton wave function in real space, including both its spatial extent and its internal phase structure. The reconstructed wave function reveals coherent delocalization across approximately three molecular units and exhibits a characteristic phase modulation, consistent with *ab initio* calculations within the framework of many-body perturbation theory. Time-resolved measurements further indicate an approximately 25% contraction of the exciton radius within 400 fs, suggesting self-trapping driven by exciton-phonon coupling. These results establish trPOT as a general and experimentally accessible approach for resolving exciton wave functions—with spatial, phase, and temporal sensitivity—in a broad class of molecular and low-dimensional materials.

DOI: 10.1103/3zmg-276c

Subject Areas: Condensed Matter Physics, Materials Science, Semiconductor Physics

I. INTRODUCTION

Excitons govern the optical response and energy transport in organic semiconductors [1,2]. While their energetic structure is well established, direct experimental access to the full quantum-mechanical exciton wave function, including its spatial envelope and internal phase, has remained out of reach. This gap is significant: The exciton wave function controls migration, dissociation, and coupling to the molecular lattice, and thus plays a central role in phenomena ranging from light harvesting [3–5] to quantum-coherent excitonics [6–8].

Here, we introduce an approach that directly measures exciton wave functions with both spatial and phase resolution using femtosecond time-resolved photoemission orbital tomography (trPOT) [9–12]. This technique combines pump-probe photoemission spectroscopy with momentum microscopy, yielding momentum-space distributions of the photoexcited state. We develop a broadly applicable model that enables the reconstruction of the exciton wave function in real space from these momentum-space signatures. In contrast to prior studies in two-dimensional semiconductors [12–17], where only the width of the momentum distribution could be linked to the exciton radius, our method retrieves the internal structure of excitons in organic semiconductors, including phase modulations between molecular units.

The model reproduces key features obtained from *ab initio* many-body perturbation theory, by solving the

*Contact author: s.tautz@fz-juelich.de

†Contact author: hoefer@physik.uni-marburg.de

‡Contact author: peter.puschnig@uni-graz.at

quasiparticle equations within the GW approximation and the Bethe-Salpeter equation for correlated electron-hole pairs, enabling a direct comparison between experiment and theory. It also provides a framework for analyzing the temporal evolution of excitons. We observe a contraction of the exciton size by roughly 25% within 400 fs, consistent with self-trapping driven by exciton-phonon coupling [18].

We use α-sexithiophene (6T) thin films as a model system. 6T is a prototypical organic semiconductor, which is relevant for optoelectronic applications such as solar cells [19], and its photophysics has been extensively studied in the past, both experimentally [20–23] and theoretically [24–26]. As substrate, we select oxygen-passivated Cu(110) which leads to the growth of uniaxially aligned molecules in a herringbone structure [27–29]. This ensures intermolecular overlap of the molecules' π electron systems, enabling exciton delocalization across multiple molecules, which is an essential condition to explore the crossover from localized Frenkel excitons to delocalized Frenkel-Wannier excitons [2,30]. This situation contrasts with earlier trPOT work on weakly coupled molecules [9], in which we have investigated flat-lying molecules with negligible intermolecular coupling, where excitations were essentially confined to single-molecule Frenkel excitons. In the present case, intermolecular overlap brings out the genuine excitonic structure, allowing us to access phase coherence and spatial delocalization across multiple molecular units.

II. RESULTS

A. Momentum mapping of the exciton

To directly observe the internal structure of an exciton, we performed ultrafast trPOT measurements on aligned 6T films using femtosecond high-harmonic probe pulses to record the momentum-space distribution and time evolution of the exciton. As illustrated in Fig. 1(a), we have prepared a sample consisting of an oriented thin film of the rodlike organic semiconducting molecule 6T, whose chemical structure is depicted in Fig. 1(b), adsorbed on the oxygen-passivated Cu(110)-(2×1)O surface. This substrate serves two important purposes. First, it electronically decouples the molecules from the metallic substrate [9], thereby preventing a rapid quenching of the exciton. Second, the (2×1) missing-row O reconstruction aligns the 6T molecules with their long axes along the $y=[001]$ direction of the Cu substrate since the molecules get trapped in the troughs between two adjacent Cu-O rows. Importantly, the molecules do not adsorb flat, but with their molecular planes tilted by approximately 32° about their long axis [29], as indicated in Fig. 1(a), thereby facilitating an effective overlap of the π electron systems between neighboring molecules. For our experiments, we have chosen a four-monolayer film in which the molecules adopt a herringbonelike arrangement with alternating tilt angles, similar to the stacking in the bulk crystal structure of 6T [31].

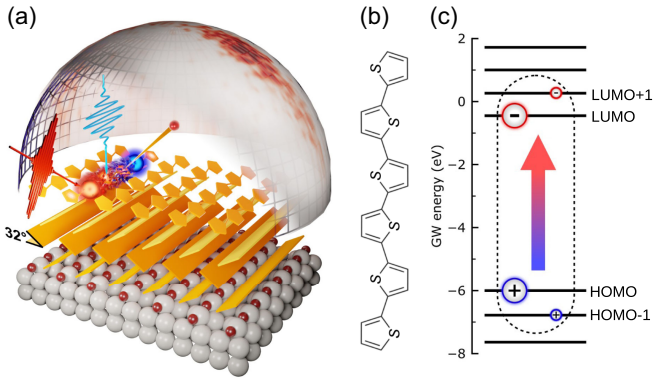

FIG. 1. (a) Structural model of four monolayers of 6T (yellow) on the Cu(110)-(2×1)O substrate in which molecular planes are tilted by $\pm32°$ with respect to the sample surface (gray, copper atoms; red, oxygen atoms). The normal-incidence pump (blue) and p-polarized probe at 55° incidence (red) pulses as well as the angular distribution of the emitted electrons are illustrated. (b) Chemical structure of 6T. (c) Illustration of the lowest optically allowed exciton state S_1 with the primary HOMO to LUMO and the secondary HOMO-1 to LUMO+1 contributions.

In order to select the photon energy and polarization direction of the pump laser pulse, we investigated the optical properties of 6T. In a first step, we performed calculations for an isolated 6T molecule employing a many-body perturbation theory approach. The resulting quasiparticle energies of the frontier molecular orbitals obtained within the GW approximation are depicted in Fig. 1(c) and show a gap of 5.3 eV between the lowest unoccupied molecular orbital (LUMO) and the highest occupied molecular orbital (HOMO). The solution of the Bethe-Salpeter equation (BSE) then reveals the energetically lowest excited state S_1 to exhibit a transition dipole moment parallel to the long axis of 6T at a transition energy of 2.8 eV. Thus, for an isolated 6T molecule a substantial exciton binding energy of 2.5 eV is to be expected. The calculations also show that, in addition to the major HOMO to LUMO contribution, there is a secondary 8% share of a HOMO-1 to LUMO+1 transition in the S_1 state, a value which is considerably smaller than an earlier prediction of 20% [32]. Importantly, however, as shown in Refs. [12,33], such an entangled excited state is predicted to exhibit a clear energy and momentum-space signature and can therefore be put to an experimental test.

Based on this analysis and on experimental optical reflection data [27], we used a normal-incidence pump pulse linearly polarized parallel to the long molecular axis for our trPOT experiments in order to maximize the transition rate into the S_1 exciton. The pump energy was chosen to be 2.35 eV in line with earlier reflectance measurements on this 6T film [27], thus somewhat smaller than the computed transition energy for the isolated molecule. The linearly polarized probe pulse (21.7 eV) created by high-harmonics generation was incident at an

angle of 55° with the electric field oriented along the [001] crystallographic direction (i.e., the y direction), thereby optimizing the photoemission cross section for molecular emission. The photoelectrons were detected with a time-of-flight momentum microscope, allowing us to record a 4D data cube $I(E_{\mathrm{kin}}, k_x, k_y, t)$. Thus, the photoemission intensity I was measured as a function of the photoelectrons' kinetic energy E_{kin}, their two parallel momentum components k_x and k_y, and the delay time t between the pump and the probe pulses, respectively. Note that in the actual analysis of the data, we reference energies to the Fermi energy E_{F}, such that an energy value of zero corresponds to electrons emitted from the Fermi level; the negative energies indicate occupied states while positive values signalize transiently excited states. Details of our experimental setup are described in Appendix A 2.

An overview of the photoemission data is given in Fig. 2(a), which shows momentum-integrated spectra at $t = 0$ fs both for occupied states below the Fermi energy E_{F} and for energies above, the latter enhanced by a factor of 1000 for the sake of clarity. Below E_{F}, we find the HOMO and HOMO-1 emissions at about -1.5 and -2.3 eV, in agreement with a previous study [28]. A momentum map taken around the HOMO peak is shown in the lower left corner of Fig. 2(b). The comparison with a simulation for a freestanding layer of 6T molecules (lower right corner) shows excellent agreement and clearly supports this assignment. It is important to note that the simulation takes into account both the polarization of the probe pulse, which is incident from the negative k_y direction and which gives rise to the "up-down" asymmetry in the maps, as well as the molecular tilt angle of $\pm 32°$ in the molecular film which has been determined by static POT [29,34].

Above E_{F}, the pump pulse creates an excitation whose photoemission signature peaks at 1.05 eV. As shown by the delay scan in Fig. 2(c), we observe a single-exponential decay with a lifetime of (422 ± 15) fs, which is somewhat larger than the 250 fs observed for a single layer of perylenetetracarboxylic dianhydride (PTCDA) molecules on the oxygen-passivated Cu(110) surface [9], presumably owing to the thicker organic film in the present case. The momentum distribution at $t = 0$ fs is shown in the top left corner of Fig. 2(b). It is characterized by two emission features (major lobes) along the $k_y = 0$ line symmetrically grouped around the $\bar{\Gamma}$ point, and another weaker, minor lobe at $k_y \approx 1.7$ Å^{-1}. In a first attempt, we associate this observed momentum pattern with the LUMO of 6T, which is depicted in the top right corner of Fig. 2(b). For simulating this map, we assumed that an electron populates the LUMO band of the freestanding 6T layer, but no interactions whatsoever with the remaining hole are considered. Such an approach has proven successful for PTCDA on oxygen-passivated Cu [9]. In contrast, the experimental map for 6T shows marked differences to the so-obtained simulated map. The map employing the independent-particle approximation is characterized by two stripelike features along k_x in the k regions of the major and minor lobes, respectively. Thus, the simulation fails to reproduce the observed intensity modulation along the k_x direction in the major lobe region, resulting in an intensity maximum at normal emission, rather than two separated peaks with a minimum at normal emission in the measurement. Moreover, the minor lobe also appears more extended in the simulation, while it is concentrated around $k_x = 0$ in the experimental map. A possible origin of this discrepancy could be that electron-hole correlations cannot

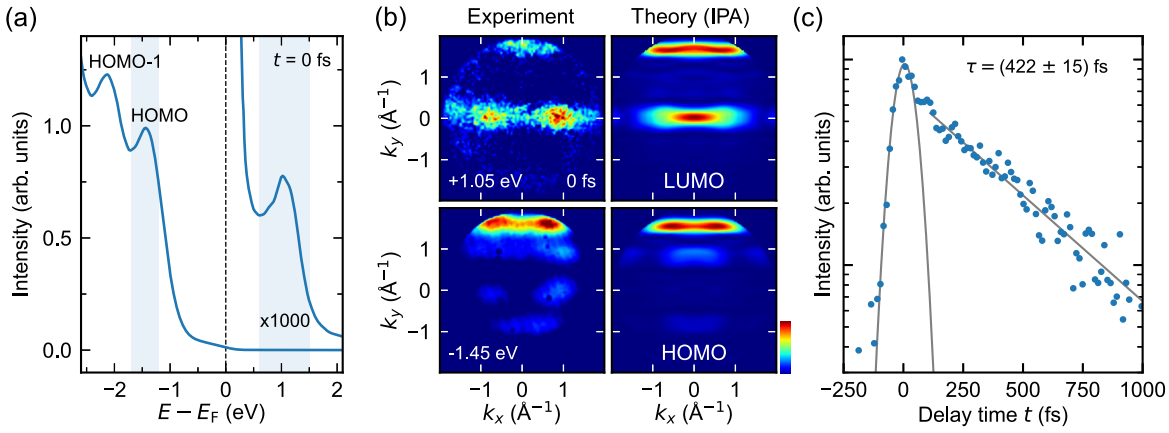

FIG. 2. (a) Momentum-integrated photoemission spectrum with molecular emission from the HOMO and HOMO-1 below the Fermi energy E_{F} and the excitonic signature above E_{F} at $t = 0$ fs. (b) Momentum maps averaged over the blue-shaded energy regions indicated in panel (a) corresponding to the HOMO (lower row) and exciton (upper row). The experimental data (left column) are compared to simulations for the HOMO and LUMO, respectively, computed in the independent-particle approximation (IPA) for a freestanding monolayer of 6T molecules. (c) Momentum-integrated intensity averaged over energies between 0.6 and 1.4 eV, as a function of delay time t indicating an exponential decay of the exciton with a lifetime of $\tau = (422 \pm 15)$ fs.

be ignored for 6T. Furthermore, it needs to be clarified whether an additional LUMO+1 contribution, as predicted for an isolated 6T molecule, could contribute to the deviation between experiment and theory regarding the momentum distribution of the excited state.

B. Exciton model

To analyze the experimental data in more detail, we employ a model exciton wave function that captures all essential physics and which allows us to extract key properties of the exciton from experimental momentum maps. To reveal the spatial extent of the exciton beyond a single molecule, we employ a linear combination of LUMOs ξ_L (of an isolated, single 6T molecule) at molecular sites $\boldsymbol{R}$ modulated by a real-valued envelope function $\alpha(\boldsymbol{R})$ and a complex, site-dependent phase factor $e^{i\beta(\boldsymbol{R})}$. This leads to the following expression that describes the probability amplitude $\psi(\boldsymbol{r}_e)$ of finding an electron with respect to a fixed-hole state (see Appendix C 1)

$$\psi(\boldsymbol{r}_e) = \sum_{\boldsymbol{R}} \alpha(\boldsymbol{R}) e^{i\beta(\boldsymbol{R})} \xi_L(\boldsymbol{r}_e - \boldsymbol{R}). \tag{1}$$

Following the approach of photoemission orbital tomography, and as detailed in Appendix C 2, we compute photoemission momentum intensity maps $I_{\mathrm{model}}(\boldsymbol{k})$ from the absolute value squared of the Fourier transform of $\psi(\boldsymbol{r}_e)$ defined in Eq. (1). It is straightforward to see that $I_{\mathrm{model}}(\boldsymbol{k})$ can then be expressed as the product of the Fourier transform $\mathcal{F}[\xi_L](\boldsymbol{k})$ of the LUMO with the Fourier series of the complex envelope function in the following way:

$$I_{\mathrm{model}}(\boldsymbol{k}) \propto \left| \sum_{\boldsymbol{R}} \alpha(\boldsymbol{R}) e^{i\beta(\boldsymbol{R})} e^{-i\boldsymbol{k}\cdot\boldsymbol{R}} \right|^2 \cdot |\mathcal{F}[\xi_L](\boldsymbol{k})|^2. \tag{2}$$

The outcome of Eq. (2) is illustrated in Fig. 3(a) for various choices of the envelope function $\alpha(\boldsymbol{R})$, the phase modulation $e^{i\beta(\boldsymbol{R})}$, and the unit-cell shape. We begin with the limiting case in which the electron is confined to a single molecule; thus, $\alpha(\boldsymbol{R})$ is sharply peaked at the central molecule $\boldsymbol{R} = 0$ and does not extend to adjacent molecules. In this Frenkel-exciton limit shown in panel (i), the sum over $\boldsymbol{R}$ collapses to a single contribution, and the resulting momentum map reduces to the one of an isolated 6T molecular LUMO $|\mathcal{F}[\xi_L](\boldsymbol{k})|^2$ shown in the top left panel of Fig. 3(a). It results in the two characteristic stripelike emission patterns discussed above. However, when allowing the electron to extend to neighboring molecules, for illustration we set $\alpha(\boldsymbol{R})$ to a Gaussian function with a full width at half maximum (FWHM_x) indicated by the black arrow in panel (ii), the stripes are modulated in a characteristic fashion. The width of the intensity maximum (FWHM_k) at the $\bar{\Gamma}$ point shown by the white arrow turns out to be inversely proportional to the real-space extension of the exciton.

Note that in panel (ii), a possible phase modulation has been ignored by setting $\beta(\boldsymbol{R}) = 0$, resulting in an intensity maximum at $\bar{\Gamma}$ in disagreement with the experimental observations. Therefore in panel (iii), we choose $\beta(\boldsymbol{R})$ such that the wave function acquires a phase flip of π between the LUMOs of adjacent molecules along the x direction. Thereby, the intensity maxima are shifted in momentum space. Along the $k_y = 0$ line, now two intensity maxima at $k_{x,\mathrm{max}} = \pm(\pi/d) \approx \pm 0.6\,\text{Å}^{-1}$ appear, where $d \approx 5.5$ Å [31] denotes the lateral spacing of two adjacent molecules in the x direction. Thus, our model already accounts for the measured intensity modulations in the major lobe region. From the experimental map [Fig. 2(b)], we extract peak maxima at $k_{x,\mathrm{max}} \approx \pm 0.85$ Å^{-1}, in reasonable agreement with the model, and a FWHM_k of 0.63 Å^{-1}. Note that the asymmetry between the left and right lobes in experiment, which is absent in the model, can be explained by residual misalignment of the sample. This assignment is supported by fact that the same asymmetry is observed in the experimental HOMO map in Fig. 2(b). Using the relation $\mathrm{FWHM}_k \times \mathrm{FWHM}_x = 8 \ln 2$ for a Gaussian, the latter translates into a real-space FWHM_x of approximately 9 Å, thus suggesting an exciton which extends over about three molecules.

Upon closer inspection of the minor-lobe region for the model result in panel (iii), however, a minimum at $k_x = 0$ is observed, while the experimental map shows a maximum. Owing to the lattice sum in Eq. (2), the exact position of intensity extrema in the minor-lobe region is sensitive to geometric details of the unit cell. In fact, choosing a vertical "slip" of 2.8 Å between neighboring molecules [indicated by the black arrows in panel (iv)], which is consistent with the bulk 6T crystal structure [31], also improves the experimental agreement of the model result in panel (iv) in this minor-lobe region with essentially no changes in the major lobe region.

C. *Ab initio* calculations

Given the success of our intuitive exciton model, we wanted to put it on firmer ground and therefore performed *ab initio* GW and BSE calculations beyond the isolated molecule limit. In particular, we treated a cluster of four 6T molecules and a periodic, freestanding monolayer of 6T molecules. The computational details of these two approaches (alongside details of additional cluster systems) are described in Appendixes B 1 and B 2, respectively. Our first observation from these *ab initio* computations pertains to the weaker LUMO+1 share to the first exciton. While for an isolated 6T molecule this contribution is 8%, it decreases with system size; thus, it reduces to 6% in the tetramer and amounts to only 3% for the extended 6T layer, a factor of 6 smaller than the earlier prediction for gas-phase 6T [32]. *A posteriori*, such a small contribution of the LUMO+1 justifies the simplified model ansatz used in Eq. (1), in

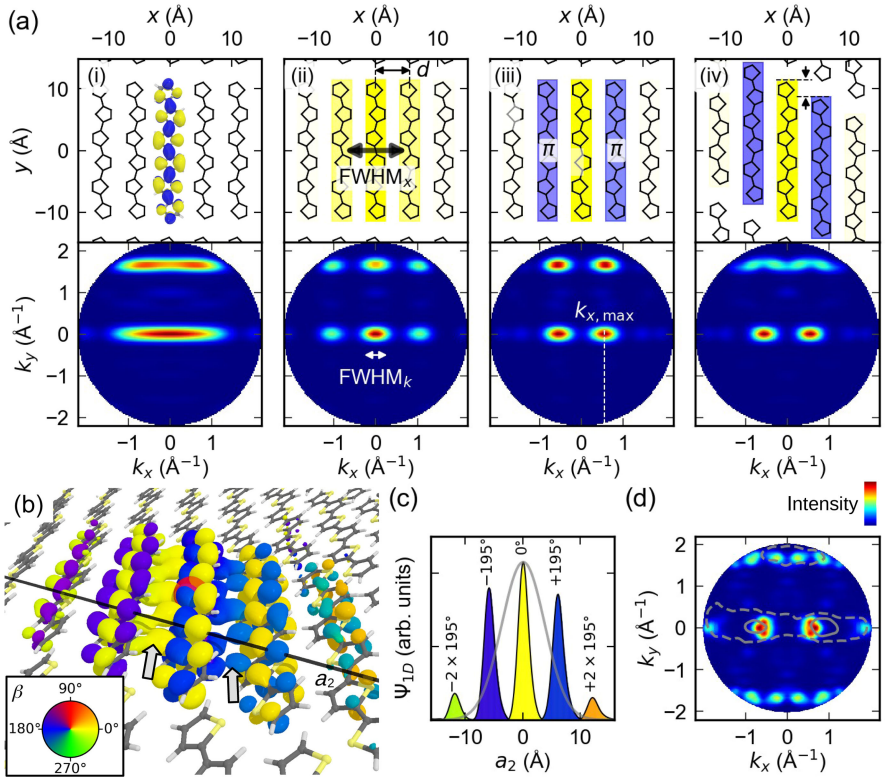

FIG. 3. (a) Illustration of the exciton model in real space (upper row) and momentum space (lower row) according to Eqs. (1) and (2), respectively. The four columns (i–iv) correspond to different choices for the envelope function $\alpha(\boldsymbol{R})$ indicated by the black arrow, the phase modulation $e^{i\beta(\boldsymbol{R})}$, and the unit-cell shape as detailed in the text. (b) Electron distribution $\Psi(\boldsymbol{r}_e, \boldsymbol{r}_h)$ of the *ab initio* exciton S_1 with respect to a fixed-hole position $\boldsymbol{r}_h$ indicated by the red sphere located at the central molecule. For the visualization of the isosurface, we have chosen a value of 10% (3.5%) of the maximum value of the absolute value $|\Psi|$ for the central three (outer two) molecules, while the phase $\arg(\Psi)$ is color coded (see color wheel in the inset). (c) One-dimensional line cut of the complex wave function $\Psi(\boldsymbol{r}_e, \boldsymbol{r}_h = \text{fixed})$ along the crystalline $\boldsymbol{a}_2$ direction [black line in panel (b)]. The solid line represents the absolute value and the filled colors the phase β, respectively. The gray line shows a Gaussian envelope based on the experimental FWHM$_x$. (d) Momentum map corresponding to exciton S_1 according to Eq. (3). The solid (dashed) gray lines are isolines of the experimental exciton map [see Fig. 2(b)] at 50% (5%) of its intensity maximum.

which only the LUMO has been considered. It also explains why experimentally no signatures of the LUMO+1 could be detected in the pump-probe photoemission data. Note that given the fact that electronic LUMO+1 contributions to the exciton wave function are connected to HOMO-1 contributions of the hole, energy conservation demands [33] that the LUMO+1 emission features are expected 0.8 eV below the peak at $E - E_F \approx 1.05$ eV [compare Fig. 2(a)]. Taking into account the rapidly rising photoemission background when approaching the Fermi level and the predicted approximately 20–30 times lower intensity than the main peak, a possible LUMO+1 contribution is therefore extremely hard to detect experimentally.]

The second finding from our *ab initio* GW and BSE calculations strengthens our model ansatz by connecting the spatial structure of the exciton wave function with certain characteristics of the momentum map. For that purpose, we focus on our results for the freestanding 6T layer and the state S_1, the major contribution of the primary absorption peak (compare Fig. 10). A common way to picture an electron-hole wave function $\Psi(\boldsymbol{r}_e, \boldsymbol{r}_h)$ is to plot the probability amplitude of finding an electron with respect to a hole fixed in space. The *ab initio* exciton wave function for S_1 is shown in Fig. 3(b), where the hole, visualized by the red sphere, has been positioned above a carbon atom connecting the central thiophene rings. Rather than showing just the absolute value $|\Psi(\boldsymbol{r}_e, \boldsymbol{r}_h = \text{const})|$, which we represent by an isosurface at 10% of the maximum value, we also visualize the color-coded phase of Ψ, an essential factor following our discussion of the model above. The wave function depicted in Fig. 3(b) allows us to make three observations. First, the exciton is indeed not constrained to a single molecule, but extends over several molecules. From the line cut along the a_2 stacking direction (compare unit cell in Fig. 8), we extract an envelope function resulting in a FWHM$_x$ of the probability amplitude of approximately 16 Å, somewhat larger than the experimental value shown as a gray line in Fig. 3(c). Second, we can clearly recognize the nodal patterns of the LUMO [see Fig. 3(a) and panel (i)]. Third,

we clearly notice a characteristic phase variation across adjacent molecules that can best be seen by inspecting the line cut through the upper half of the molecular π orbitals shown in Fig. 3(c). Specifically, the phase changes by $\Delta\beta \approx 195°$ when moving from the central molecule to the right or left, respectively, thus by a value close to the phase flip of π assumed in panels (iii) and (iv) of Fig. 3(a) in our model exciton wave function. Note that this phase relationship between adjacent molecules' LUMO orbitals results in a bonding intermolecular combination at their region of overlap indicated by the arrows in Fig. 3(b). It is worth mentioning that our GW and BSE calculations also predict an energetically higher lying, also optically active, S_3 state with a different phase relation that leads to an antibonding intermolecular overlap between the three central molecules (compare Fig. 9).

To obtain a momentum map of the S_1 exciton calculated from the *ab initio* exciton wave function, we have extended the exciton photoemission orbital tomography (exPOT) approach [33] to periodic systems, allowing us to address excitons in the extended 6T layer studied here (see Appendix B 2). Owing to the negligible contributions of unoccupied states above the LUMO to S_1, the general expression for photoemission intensity $I(\boldsymbol{k})$ [see Eq. (B6)] reduces to a simple product between the eigenvector of the effective electron-hole BSE Hamiltonian $X^{S_1}_{v_1 c_1 \boldsymbol{k}}$ and the Fourier transform of the lowest conduction-band orbital $\mathcal{F}[\xi_{c_1 \boldsymbol{k}}]$ [see Eq. (C23)],

$$I_{S_1}(\boldsymbol{k}) \propto \left| X^{S_1}_{v_1 c_1 \boldsymbol{k}} \right|^2 \cdot |\mathcal{F}[\xi_{c_1 \boldsymbol{k}}]|^2. \tag{3}$$

Thus, the overall structure of this *ab initio* expression for the photoemission intensity closely resembles the one of the model exciton wave function, Eq. (2), further justifying the model. The Fourier transform of the LUMO $\mathcal{F}[\xi_L]$ should be identified with the Fourier transform of the lowest conduction state c_1, $\mathcal{F}[\xi_{c_1 \boldsymbol{k}}]$, and the lattice sum appearing in Eq. (2) corresponds to the momentum-space representation of the BSE eigenvector $X^{S_1}_{v_1 c_1 \boldsymbol{k}}$ for the respective exciton S_1. Details on the relation between the exciton model and the first-principles description can be found in Appendix C, where direct comparisons of the model predictions with the *ab initio* results are shown in Figs. 13 and 14 for excitons S_1 and S_3, respectively.

The map resulting from the *ab initio* approach, Eq. (3), is depicted in Fig. 3(d) and agrees well with both the model result (iv) and the experimental momentum map whose main intensity features are included as gray isolines in Fig. 3(d). In particular, also the *ab initio* map exhibits pronounced intensity maxima along the major lobe region, whose widths FWHM_k are consistent with the FWHM_x of the envelope of the exciton and whose k_x positions are related to the abovementioned phase modulation with $\Delta\beta \approx 195°$. Using $\lambda = [360°/(\Delta\beta)]d$, with d denoting the molecular spacing (see Fig. 8), explains the appearance of the maxima at $k_{x,\mathrm{max}} = \pm[2\pi/\lambda] \approx \pm 0.64$ Å^{-1}.

While both the exciton model and the monolayer *ab initio* calculation qualitatively reproduce the experimental momentum pattern, there remains a small deviation regarding the position of the maxima, for which experimentally a value of $k_{x,\mathrm{max}} \approx \pm 0.85$ Å^{-1} is found. We attribute this difference to the simplified structural model consisting of only a single 6T layer, while the experiment is performed on four layers of 6T. Unfortunately, *ab initio* GW and BSE calculations for such a four-layer periodic structure are out of reach for computational reasons. Thus, we checked the influence of a second 6T layer by performing cluster calculations for a 6T hexamer containing three molecules in the first and three in the second layer (see Appendix B). These computations lead to a momentum map exhibiting the characteristic double-lobe structure along $k_y = 0$ that was already seen in the momentum map of a single layer, however with a small change in $k_{x,\mathrm{max}}$ [Fig. 11(e)]. These additional results therefore indicate that the presence of the second layer may indeed affect the intermolecular phase slip slightly and thus the position of the maxima. At the level of the model, the extension to a multilayer would introduce additional free parameters controlling the interference between the layers that would have to be chosen with care. To keep the discussion of the model and its parameters as simple as possible, and also safeguard the possibility of directly verifying the influence of its parameters on momentum patterns via comparison to *ab initio* GW and BSE calculations, we have therefore restricted ourselves to a monolayer model and leave an extension to a multilayer model for future work.

D. Time evolution of an exciton

Utilizing the exciton model, we are in a position to extract the temporal evolution of the exciton wave function from the experimentally observed delay-time dependence of the momentum signatures depicted in Fig. 4. Figure 4(a) shows experimental momentum maps of the S_1 exciton at $+1.05$ eV above E_F for five different delay times. We now analyze the major lobe region (red boxes) in more detail by plotting intensity linescans along k_x shown as black lines in the lower row of Fig. 4(a). According to our exciton model, we fit the linescans by two Gaussians with in total five adjustable parameters, namely, one common FWHM_k and two independent peak positions [$k^-_{x,\mathrm{max}}$ and $k^+_{x,\mathrm{max}}$, with Fig. 4(b) showing $\bar{k}_{x,\mathrm{max}} = \frac{1}{2}(|k^-_{x,\mathrm{max}}| + k^+_{x,\mathrm{max}})$] and peak heights to account for the asymmetry in the experimental data which arises from a slight misalignment of the sample. The resulting best fits and the statistical uncertainties of the fit parameters are depicted in Fig. 4(b).

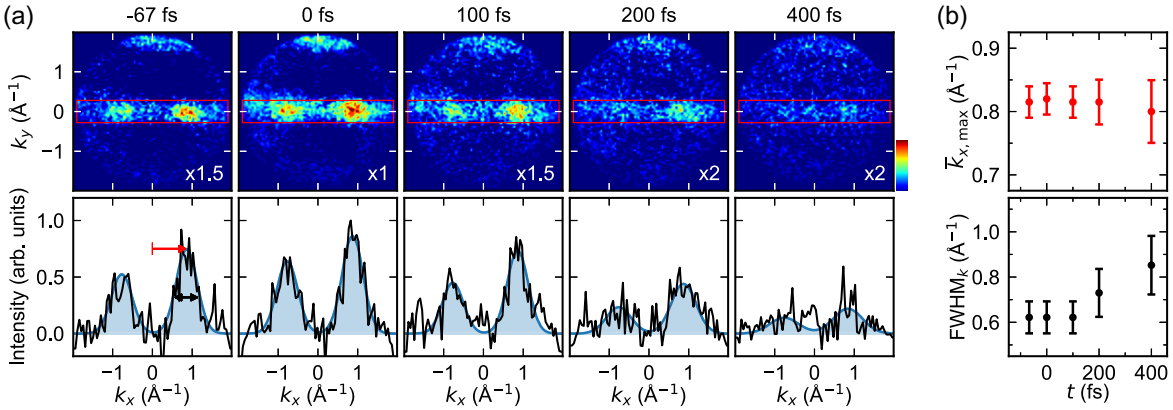

FIG. 4. (a) Experimental momentum maps at five different pump-probe delay times t (upper row), together with intensity linescans (lower row) extracted along k_x in the red-boxed regions. The blue-shaded areas correspond to fits to the extracted linescans (black lines) using two independent Gaussians with one common FWHM$_k$. (b) Position (red symbols) and FWHM$_k$ (black symbols) of the intensity peaks as a function of the delay time resulting from the fits shown in panel (a).

First, the results indicate an increase of the FWHM$_k$ from (0.63 ± 0.07) Å^{-1} at $t = 0$ fs to about (0.85 ± 0.13) Å^{-1} at 400 fs, which translates into a localization of the real-space exciton envelope from initial (8.8 ± 1.0) to (6.5 ± 1.0) Å. Such a localization is expected to be accompanied by a slight increase in the exciton binding energy, consistent with our experimental data (see Fig. 7 in Appendix A 5), and may arise from polaronic effects due to exciton-phonon coupling. A comprehensive microscopic theory of exciton-phonon coupling that could account for our experimental findings lies beyond the scope of this study. Nevertheless, the combination of time-resolved momentum imaging and our model introduces a new set of measurable observables that offer a solid benchmark for future theoretical work. Second, within statistical uncertainties, the position of the intensity maxima $k_{x,\max}$ remains nearly constant over time, reflecting the fact that the phase modulation retains the bonding character during the entire lifetime of the exciton. Together, these findings establish a direct experimental view of both the spatial extent and internal phase coherence of excitons, and how these evolve under the influence of exciton-phonon coupling.

As a final note, our data in Fig. 7 indicate—in addition to the abovementioned minor energy shift of the primary exciton peak around 1.05 eV—the appearance of a second exciton species at the considerably lower energy of 0.6 eV at later times, which could be due to a dark exciton state. Indeed, in our GW and BSE calculations for 6T clusters (see Appendix B 1), we observe the appearance of optically dark excitons energetically below the first optically allowed peak consistent with well-known Davydov splitting. We obtain energy splittings ranging from 0.3 eV (trimer) to 0.5 eV (hexamer). As can be observed from the momentum-integrated energy spectra depicted in Appendix A 5 (Fig. 7), the experimentally observed species appearing at 0.6 eV could indeed signal the presence of a dark exciton which gets populated at later times. Importantly, however, this dark exciton species at 0.6 eV does not affect our argument for the time-dependent contraction of the bright exciton at 1.05 eV, since the latter emission feature is energetically well separated from the dark exciton. As a result, the momentum distribution for the bright exciton at 1.05 eV remains essentially unaffected by the lower-lying dark exciton. In our analysis of the experimental data, we have verified this by reducing the energy integration window for obtaining the momentum maps, revealing that the results of the Gaussian fitting remain essentially unaltered.

III. CONCLUSION

We have introduced a general method for reconstructing exciton wave functions from time-resolved momentum-resolved photoemission measurements. Applied to α-sexithiophene, this approach reveals both the spatial delocalization and internal phase structure of the exciton, in agreement with GW and BSE calculations. The observed coherent extension across three molecular units and the characteristic phase modulation demonstrate the mixed Frenkel-Wannier nature of the exciton in this system. Time-resolved measurements further indicate an approximately 25% reduction in exciton size within 400 fs, suggesting self-trapping facilitated by exciton-phonon coupling. This capability to track both the spatial and temporal evolution of the exciton wave function represents a substantial advance beyond envelope-function imaging in two-dimensional materials. Because the method relies on general features of the photoemission process and does not assume system-specific simplifications, it provides a widely applicable framework for visualizing excitonic correlations in molecular, hybrid, and low-dimensional materials. It thus opens new opportunities for probing many-body quasiparticle dynamics and for benchmarking theoretical approaches to correlated electron-hole pairs.

ACKNOWLEDGMENTS

We acknowledge support from the European Research Council, Synergy Grant "Orbital Cinema," Project ID No. 101071259 and the Deutsche Forschungsgemeinschaft (DFG, German Research Foundation) through SFB 1083, Project-ID No. 223848855. The computational results have been achieved using the Austrian Scientific Computing infrastructure.

F. S. T., U. H., and P. P. conceived and designed the research. M. S. and E. F. prepared the α-sexithiophene samples with support from F. C. B. and S. S. The time-resolved photoemission experiments where performed by M. T. and M. S.; E. F., F. C. B., and A. A. assisted in carrying them out. S. Z., R. W., and U. H. designed and constructed the experimental setup. S. K., with support from C. K. and A. W., performed the *ab initio* GW and BSE calculations. S. K. analyzed all theoretical data and prepared the corresponding figures. M. T. analyzed all experimental data and prepared the time-resolved POT figures. A. W. and M. G. R. proposed the studied system. F. S. T., U. H., and P. P. supervised the Ph.D. work of M. S., M. T., and S. K., respectively. P. P. wrote the manuscript with significant input from M. T., S. K., M. G. R., F. S. T., and U. H. All authors discussed the results, contributed to the interpretation, and reviewed and improved the final manuscript and figures.

There are no competing interests to declare.

DATA AVAILABILITY

All raw experimental data and computational data generated and analyzed in this study are publicly available from the Jülich DATA repository [35]. For the *ab initio* electronic structure calculations, the repository additionally includes the input files and the most relevant output files required to reproduce the reported results.

APPENDIX A: MATERIALS AND EXPERIMENTAL METHODS

1. Sample preparation

The sample preparation was performed in ultrahigh vacuum (UHV) with a base pressure in the low 10^{-10}-mbar range. After repeated cycles of Ar sputtering ($P_{\mathrm{Ar}} = 1 \times 10^{-5}$ mbar; $E = 1$ keV; 30 min) and annealing (600 °C; 30 min), the Cu(110) substrate was heated to 300 °C (measured with a DIAS Pyrospot DP 10N pyrometer with $\epsilon = 0.05$) and exposed to oxygen at 1×10^{-7} mbar for 10 min. This resulted in the well-known $p(2 \times 1)$ oxygen reconstruction, wherein the oxygen atoms are arranged in rows along the [001] direction [36]. This reconstruction emerges as alternating stripes of bare Cu(110) and (2×1)O-reconstructed Cu(110), where increased exposure leads to wider Cu-O regions [37]. Conversely, overexposure to oxygen leads to the formation of another oxygen-induced reconstruction, namely, $c(6 \times 2)$ [36]. Thus, the exposure time was set as high as possible so that no indications of the $c(6 \times 2)$ structure arose in low-energy electron diffraction (LEED).

Before use in our experiments, the 6T molecules (Tokyo Chemical Industry Co. Ltd.) were purified by sublimation. The deposition of the 6T molecules onto the substrate kept at −5 °C was done using a well-degassed Kentax three-cell evaporator operated at 250 °C. The evaporation rate was calibrated with LEED using the findings in Ref. [38].

2. Time- and angle-resolved photoemission spectroscopy experiments

The laser setup used for the time-resolved, angle-resolved photoemission spectroscopy experiments is based on a Ti:sapphire regenerative amplifier operated at 200 kHz, which delivers 800-nm laser pulses with 40-fs duration and 8-μJ pulse energy, which were split into a pump and a probe branch in a 70:30 ratio.

The pulses in the probe branch were further amplified by a two-pass amplifier and subsequently frequency doubled to 400 nm, resulting in a pulse duration of about 60 fs and a pulse energy of 1.5 μJ. For the generation of high harmonics, the pulses were tightly focused with an achromatic lens ($f = 60$ mm) into a krypton gas jet, which was produced inside a UHV chamber (10^{-8} mbar without gas load) by injecting pressurized krypton (4 bar) through a ceramic nozzle with a diameter of 30 μm. To separate the seventh harmonic (57 nm, 21.7 eV) from the residual harmonics, two wavelength-selective multilayer mirrors were used, yielding an almost isolated seventh harmonic. In addition, the two multilayer mirrors were used to collimate and refocus the p-polarized probe pulses onto the sample, after first passing through a 100-nm-thin Al filter to remove the residual 400-nm fundamental wavelength. The linearly polarized probe pulses are incident on the sample at an angle of 55°, with the electric field oriented along the [001] crystallographic direction.

For optical excitation of the 6T molecules, the pump pulses were frequency converted to 528 nm (2.35 eV) using an optical parametric amplifier, resulting in a pulse duration of 45 fs. After passing a linear delay stage, which delays the pump pulses relative to the probe pulses, they were focused onto the sample under normal incidence in order to have the linearly polarized pump pulses aligned along the long molecular axis of 6T. However, the resulting noncollinear pump-probe geometry introduces a spatial tilt between both pulse fronts and thus leads to a broadening of the temporal overlap. To compensate for this effect, the pulse fronts of the pump pulses were tilted by focusing the beam with a lens ($f = 500$ mm) onto an optical grating ($f_{\mathrm{gr}} = 1200$ g/mm) and subsequently imaging the diffracted spot onto the sample using an additional lens

($f = 250$ mm). Note that with these settings we achieve a pump fluence at the sample of approximately 50 $\mu J/cm^2$. A corresponding estimate of the exciton density is challenging, as it would require knowledge of both the quantum efficiency and the absorption cross section of the molecular layer, which cannot be reliably determined in our case. Nevertheless, a rough estimate yields an excitation density on the order of 7.8×10^{10} excitons per cm^2, a value which we estimate from the 1:1000 ratio observed for the k-integrated photoemission intensities of the exciton with that of the HOMO [compare Fig. 2(a)] and the molecular area density of 0.78 molecules/nm^2.

During the measurements, the sample was under UHV conditions ($< 2 \times 10^{-10}$ mbar) and was continuously cooled to $T_s = 24$ K with a closed-cycle helium cryostat for periods of typically ten days. The photoemitted electrons were projected by a momentum microscope—using a lens system similar to the ones used for photoemission electron microscopy—onto a time- and position-sensitive delay-line detector after passing though a 1-m drift tube. By measuring for each pump-probe delay time t the time of flight τ of the photoelectrons as well as the photoelectron intensity I and the position on the detector, which corresponds to the electrons' k_x, k_y components, we obtain—after converting the time of flight τ into a binding energy $E - E_F$—a four-dimensional dataset $I(E - E_F, k_x, k_y, t)$. The energy resolution of our momentum microscope was about 150 meV, and the momentum resolution was better than 0.01 $Å^{-1}$. Low-energy electrons were suppressed by applying a retarding field in front of the delay-line detector. The momentum maps shown in this paper were accumulated for about 25 hours for each delay time. During a single delay scan, each data point was accumulated for about 7 min.

3. Pump-induced background signal

During the measurements, a small pump-induced background signal was observed that slightly affected both the recorded energy spectra and the momentum-resolved signatures. First, by comparing the energy spectra obtained with the optical pump pulse at different delay times to a reference spectrum acquired without the pump pulse, a small time-dependent energy shift can be identified by fitting the Fermi edge for all spectra. The magnitude of this shift measured at the Fermi energy reaches its maximum of about $\Delta E = +0.02$ eV at $t = 0$ fs. To correct for this effect, the Fermi edge was fitted for each delay time and the spectra were realigned accordingly [see Fig. 5(a)]. However, in addition to this dynamic shift, a static energy shift remains that becomes increasingly noticeable at higher binding energies. This residual shift can be observed in Fig. 5(a), where the peak positions of the HOMO and HOMO-1 levels of the spectra with the pump pulse exhibit a small but systematic displacement relative to the reference spectrum. Since this effect mainly develops toward larger binding energies (0.015 eV at the HOMO and 0.045 eV at the HOMO-1), we assume that the energy region relevant for our analysis (0.6–1.5 eV) exhibits no, or at most a negligible, remaining energy shift.

Second, besides the energy shift, an additional background signal appears at the $\bar{\Gamma}$ point which extends across the entire energy spectrum, as depicted in Fig. 5(b). Because of its small magnitude, this background is clearly visible only for the unoccupied states, where it exhibits an approximately uniform intensity contribution around the $\bar{\Gamma}$ point [see Fig. 5(c), upper panel].

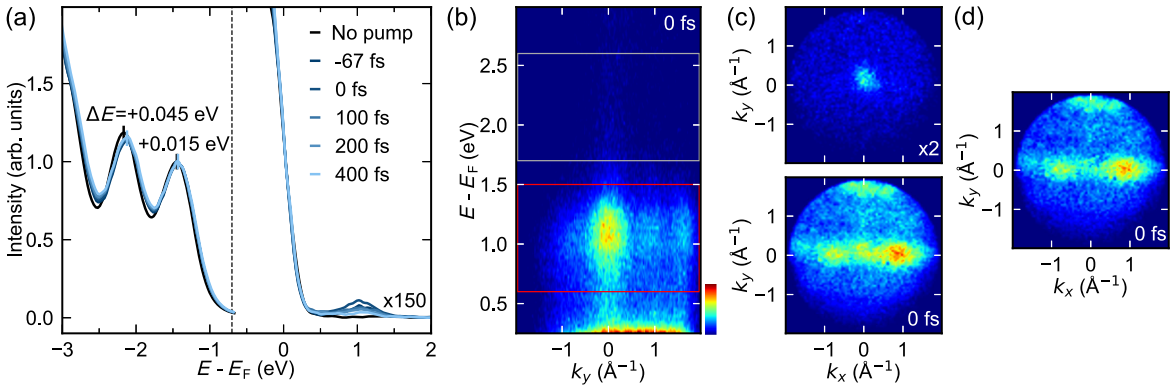

FIG. 5. (a) Momentum-integrated photoemission spectra acquired without (black curve) and with optical pump (blue curves) at five different pump-probe delay times. All spectra are corrected for the time-dependent energy shift by fitting the Fermi edge and shifting the spectra accordingly. (b) Experimental $I(E, k_y)$ map depicted at a pump-probe delay time of $t = 0$ fs and integrated within $k_x \in [-2, 2]$ $Å^{-1}$, showing the exciton signal around $E - E_F = 1.05$ eV as well as the pump-induced background signal at the $\bar{\Gamma}$ point. (c) Momentum maps of the background signal (upper panel) and the exciton (lower panel) extracted within the energy windows indicated by the gray and red boxes in (b), respectively. (d) Momentum map of the exciton after subtracting the pump-induced background signal.

Consequently, it adds a weak contribution to the momentum signature of the exciton [see Fig. 5(c) lower panel]. To account for this, we remove this background signal by subtracting its momentum signature integrated within $E - E_F \in [+1.7, +2.6]$ eV from the excitonic momentum signature obtained between $E - E_F \in [+0.6, +1.5]$ eV.

4. Background subtraction for linescans

In the experiment, the observed exciton signatures appear close to the Fermi edge, which can be seen in the momentum maps in Fig. 6(a), extracted in the energy range $E - E_F \in [+0.6, +1.5]$ eV for different delay times. Therefore, it must be noted that these momentum maps contain not only the exciton signatures, but also a background originating from the Fermi edge. In order to perform a meaningful analysis of the intensity modulation in the exciton momentum maps according to our exciton model, prior subtraction of this background is required.

First, we isolate intensity linescans along k_x in the major lobe region in Fig. 6(a) (red boxes, $k_y = \pm 0.28$ Å^{-1}) for every delay time. Similarly, we obtain intensity linescans from the momentum maps of the Fermi edge, including energies in the range $E - E_F \in [-0.4, +0.4]$ eV, again for every delay time. To ensure a statistically reliable background subtraction, the background caused by the Fermi edge was obtained from the same data cube (but in the lower energy range $[-0.4, +0.4]$ eV) rather than from a measurement recorded in the same energy range $[+0.6, +1.5]$ eV as the signal, but without the pump pulse. This approach was chosen because the data acquired without the pump pulse exhibit insufficient statistics of the count rate in the momentum map, making them unsuitable for accurate background determination. In contrast, since the momentum distribution of the Fermi edge is nearly identical in both energy regions—apart from variations in the intensity—the $[-0.4, +0.4]$ eV data recorded with the pump pulse and separately for every delay time provides improved statistics and thus a more robust background subtraction for our analysis.

We extract the background from the Fermi-edge region ($E - E_F \in [-0.4, +0.4]$ eV), where no excitonic signal is to be expected. Specifically, we take the linescans along k_x averaged over the red boxed area of the momentum map labeled "Fermi edge" in Fig. 6(a). For the background-subtraction procedure as depicted in Fig. 6(b), the Fermi-edge signal (gray) is fitted to the extracted linescans (black) using a scaling factor, while the remaining uncertainty with respect to the "real" background is accounted for by an adjustable offset. The fit is performed by minimizing the mean-square error between the gray and black curves, considering only the momentum range $|k_x| > 1.5$ Å^{-1}, where the excitonic contribution is negligible, thereby

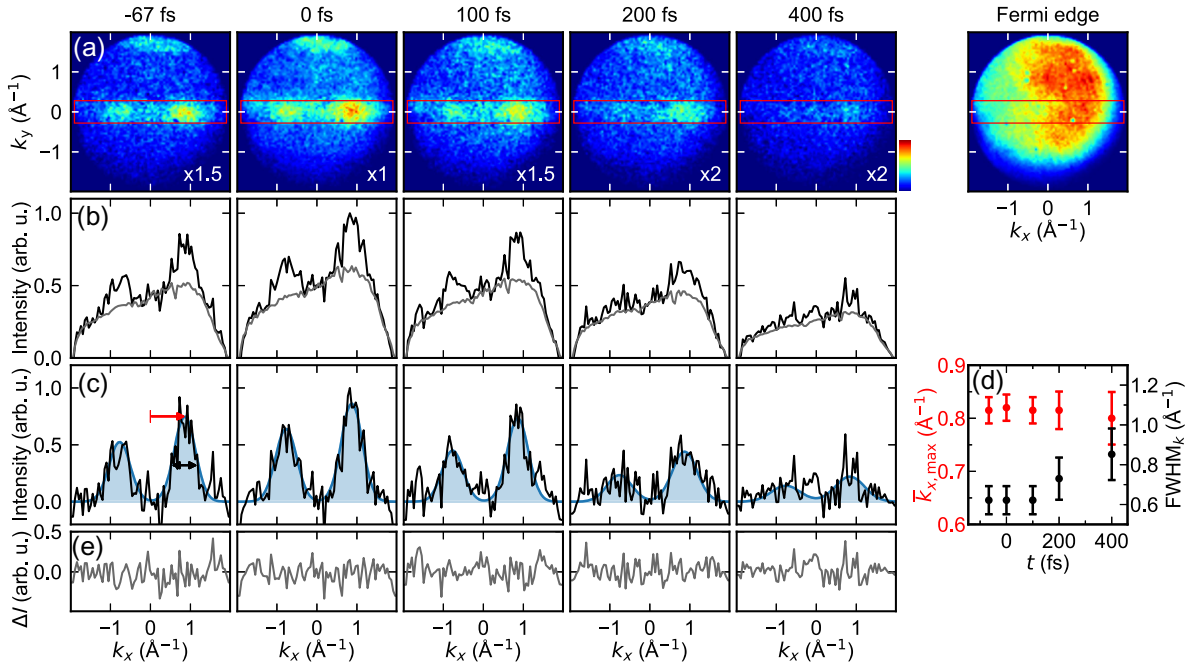

FIG. 6. (a) Experimental momentum maps at five different pump-probe delays extracted in the energy range of $E - E_F \in [+0.6, +1.5]$ eV, together with an exemplary momentum map of the Fermi edge at $t = -67$ fs, integrated over $E - E_F \in [-0.4, +0.4]$ eV. (b) Intensity linescans (black) along k_x for each delay time extracted within the red boxes in panel (a), together with fitted linescans of the Fermi edge (gray). (c) Background-subtracted linescans (black) fitted by two independent Gaussians with one common FWHM$_k$ (blue-shaded area). (d) Resulting fit parameters of the FWHM$_k$ and mean peak position as a function of the delay time, together with their statistical uncertainties. (e) Residuals between background-subtracted linescans and fitted Gaussians.

preventing the background determination from being biased by the excitonic signal.

The resulting background-subtracted linescans are displayed in Fig. 6(c) together with a fit function (blue-shaded area). According to our exciton model, the fit function consists of two Gaussians with five adjustable parameters: two peak positions $k^{-}_{x,\mathrm{max}}$ and $k^{+}_{x,\mathrm{max}}$, two amplitudes (to allow for a small misalignment of our sample), and one common FWHM_k. For this second fitting step, the background parameters obtained from the background determination—namely, the scaling factor and offset—were kept fixed. However, to assess the influence of the background determination on the extracted exciton parameters, the background parameters were systematically varied within reasonable bounds, and the resulting peak positions and FWHM_k were reevaluated. If these variations led to deviations exceeding the confidence intervals obtained from our fit function, the reported uncertainties of the peak positions and FWHM_k were increased accordingly to account for the additional systematic uncertainty introduced by the background determination. The obtained fit parameters and their statistical uncertainties are presented in Fig. 6(d). Note that $\bar{k}_{x,\mathrm{max}} = \frac{1}{2}(|k^{-}_{x,\mathrm{max}}| + k^{+}_{x,\mathrm{max}})$ here corresponds to the mean value of the two fitted peak positions. The residuals between background-subtracted linescans and the fit function are displayed in Fig. 6(e). Further analysis of the data, as well as a compressed version of Fig. 6 is provided in the main text (see Fig. 4). Note, however, that in the case of Fig. 4 the Fermi edge has already been subtracted from the displayed exciton momentum maps. For this, we used the same parameters (scaling factor, offset) as for the background subtraction in the linescans.

5. Temporal evolution of exciton energy

The analysis of background-subtracted linescans performed within the framework of our exciton model reveals a temporal increase in the FWHM_k from $t = 0$ fs to $t = 400$ fs, implying a progressive localization of the exciton wave function. This reduction of spatial extent should likewise be observable in the energy spectrum as an increase of the exciton binding energy and a concomitant decrease of the excited-state energy over time. Note that a decrease of the excited-state energy also corresponds to an energy shift toward lower final-state (kinetic) energies in a two-photon photoemission experiment. In Fig. 7(a), we therefore plot for different delay times the energy spectrum extracted from the same k region (red boxes) as depicted in Fig. 6(a). To identify a possible shift of the excited-state energy, we first subtract the Fermi edge (black curve) for all delay times, resulting in the background-subtracted energy spectra in Fig. 7(b). To account for small pump-induced energy shifts, the Fermi edge was fitted individually for each delay step (see Appendix A 3).

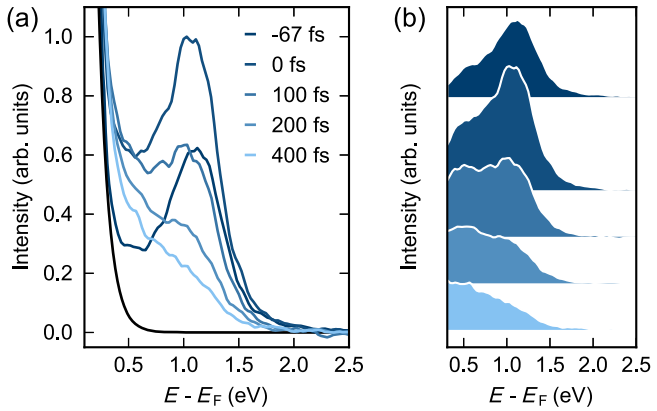

FIG. 7. (a) Energy spectra extracted within the k region defined by the red boxes in Fig. 6(a), showing the exciton signal at five different pump-probe delays, along with the Fermi edge (black) fitted individually for each delay time. (b) Remaining energy spectra of the exciton after subtraction of the Fermi edge.

A closer inspection of the energetic position of the exciton in Fig. 7(b) indeed reveals a distinct temporal evolution of the excitonic features. Between $t = -67$ and 100 fs, the spectra clearly show the optical excitation of the bright $S1$ exciton at an energy of approximately 1.05 eV, accompanied by the emergence of an additional contribution around 0.6 eV. We interpret this lower-energy feature as a population transfer into an optically dark exciton that arises from a Davydov splitting in the molecular solid. In addition to this population transfer, a small energy relaxation at early delay times can be observed, which we attribute to the optical excitation of the exciton being slightly above resonance. This process is also observed in the momentum-integrated intensity of the exciton as a function of the delay time in Fig. 2(c), where for early delay times ($t = 0$–100 fs) a fast-decaying component due to an off-resonant excitation dominates the signal, whereas at later delay times ($t = 100$–1000 fs) the slower component due to the transiently populated exciton takes over. For delay times $t > 100$ fs, the spectra indicate a continued population transfer into the lower-energy, optically dark state together with a small additional shift of the bright $S1$ exciton toward lower final-state energies. We attribute this latter shift to an increase of the exciton binding energy accompanied by a reduction of the spatial extent of the exciton wave function over time, which ultimately supports our conclusions from the background-subtracted linescan analysis.

APPENDIX B: COMPUTATIONAL METHODS

1. *Ab initio* calculations for clusters

In this section, we provide details of our GW and BSE calculations for an isolated 6T molecule, a cluster containing three and one containing four molecules, as well as for a cluster of six molecules. The geometries of the monomer,

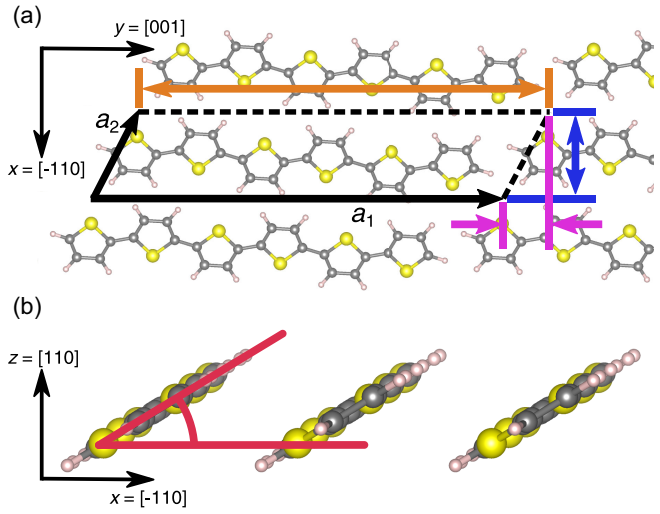

FIG. 8. (a) Top-down view of the monolayer: The unit-cell vectors are shown in black, where a_2 determines the row slip (purple) of 2.807 Å. The row distance d (blue) equals 5.335 Å, and the unit-cell length (orange) is 25.258 Å. (b) Side view of the monolayer: The molecules are tilted (red) by 31.5° relative to the x-y plane.

trimer, and tetramer system were obtained by cutting out one, three, and four molecules along the a_2 direction from the periodic monolayer shown in Fig. 8, such that these can be regarded as monolayer clusters. In contrast, the hexamer cluster is a bilayer cluster. In its first layer, it is simply the trimer system mentioned before. To these three molecules, we then added three additional molecules as a second layer based on the herringbonelike arrangement found experimentally in Ref. [31]. That is, for each molecule of the first layer (rotated by $+31.5°$ against the layer plane), we created a molecule in the second layer which is rotated by $-31.5°$ against the layer plane and shifted by about half the cell length in the a_2 direction ($0.49|a_2|$) and by 3.785 Å in the z direction [see Fig. 11(j)].

In a first step, we performed single-point ground-state density-functional-theory (DFT) calculations using ORCA 5.0.4 [39,40] with the 6-311G* Gaussian-orbital basis set [41,42] and the B3LYP hybrid functional [43,44]. The resulting Kohn-Sham orbitals and energies then served as the basis for the GW calculation. For the second step, we employed the FIESTA code [45]. Specifically, we performed an iterative, self-consistent correction of the Kohn-Sham energies while keeping the wave functions unchanged. For a single 6T molecule, we explicitly corrected ten occupied (valence) and ten unoccupied (conduction) orbitals. Orbitals beyond there were rigidly shifted by the correction that was applied to the HOMO-9 and LUMO+9. For the trimer, tetramer, and hexamer calculation, we explicitly corrected 30, 40, and 60 occupied and 30, 40, and 60 unoccupied orbitals.

In the third step, we solved the BSE in which excited states were described as correlated electron-hole pairs [46,47]

$$\sum_{v'c'} H_{vc,v'c'} X^m_{v'c'} = \Omega_m X^m_{vc}. \tag{B1}$$

Here, the eigenvalues Ω_m of the effective electron-hole Hamiltonian are the system's charge-neutral excitation energies, and the eigenvectors X^m_{vc} encode the entangled nature of the electron-hole state, which can be expressed via the exciton wave function as

$$\Psi_m(\boldsymbol{r}_e, \boldsymbol{r}_h) = \sum_{vc} X^m_{vc} \varphi^*_v(\boldsymbol{r}_h) \xi_c(\boldsymbol{r}_e). \tag{B2}$$

Using again the FIESTA code, we iteratively diagonalized the BSE Hamiltonian. This way, we calculated the first 20 excited states of the monomer, trimer, and tetramer system, where we constructed the BSE Hamiltonian by including all valence orbitals up to 20 eV below the HOMO and all conduction orbitals up to 20 eV above the LUMO. This resulted in the use of 72 valence and 135 conduction orbitals in the single-molecule calculation, 218 valence and 381 conduction orbitals in the trimer calculation, and 291 valence and 507 conduction orbitals in the tetramer calculation. Similarly, for the hexamer system we calculated the first 60 excited states, where we used 10 eV as the orbital-inclusion cutoff, leading to the inclusion of 281 valence orbitals and 319 conduction orbitals. Note that this smaller cutoff was chosen for computational reasons. Tests with the trimer system showed that using this smaller cutoff did not lead to significant changes in the momentum maps of low-lying excited states. In particular, this applies to those excitons dominated by HOMO to LUMO contributions, which are the excitons of interest here, and where we identify the first three valence and conduction orbitals of the trimer with the monomer's HOMO and LUMO. This demonstrates that the use of this somewhat smaller cutoff value for the hexamer system is well justified. In all cases, we used the Tamm-Dancoff approximation, since test calculations with the monomer showed deexcitations to contribute less than 1% to the BSE eigenvector.

In the final step, we simulated photoemission momentum maps from excitons using the exPOT approach described previously [33]. Denoting the energy of the probe laser as ω and the kinetic energy of the photoelectron as E_{kin}, the intensity of photoemission from exciton m as a function of the photoelectron momentum $\boldsymbol{k}$ is given by [33]

$$I_m(\boldsymbol{k}) \propto \sum_v \left| \sum_c X^m_{vc} \mathcal{F}[\xi_c](\boldsymbol{k}) \right|^2 \cdot \delta(\omega + \Omega_m - \varepsilon_v - E_{\mathrm{kin}}). \tag{B3}$$

The formula shows that the hole state enters the energy conservation term via its single-particle energy ε_v, while the angular distribution is determined by a coherent sum of the Fourier transforms $\mathcal{F}$ of the electron orbitals contributing to the exciton with weights X^m_{vc}. Note that in Eq. (B3) the polarization factor $|\boldsymbol{A} \cdot \boldsymbol{k}|^2$ has been omitted.

2. *Ab initio* calculations for a periodic 6T layer

This section summarizes details of our *ab initio* GW and BSE calculations for a freestanding, periodic monolayer of 6T. Its geometry is based on the experimentally determined structure of a 6T crystal [31]. We use a skewed unit cell containing one molecule per cell as depicted in Fig. 8. Just as in the cluster case, we perform a series of DFT, GW, and BSE calculations to get all the quantities required by the exPOT formalism, Eq. (B6).

For the first step, the ground-state DFT calculations, we used QUANTUM ESPRESSO (PWSCF v.7.2) [48–50], employing the Perdew-Burke-Ernzerhof (PBE) functional [51] and a plane-wave energy cutoff of 70 Ry for wave functions and 280 Ry for the density. To avoid spurious interactions between repeated slabs in the z direction, the unit-cell height was set to 28.525 Å, which corresponds to a vacuum layer of 25.521 Å. Additionally, we employed a truncation scheme for the Coulomb interaction [52]. For this and all upcoming steps, unless stated otherwise, we utilized a $2 \times 8 \times 1$ k mesh.

Steps two and three, the GW and BSE calculations, were performed using BERKELEYGW4.0 [46,53,54]. Before performing the GW step, we employed BERKELEYGW's PARABANDS tool to calculate stochastic conduction pseudobands [55] to reduce the calculation times and the scaling of the subsequent GW and BSE calculation. We protected 27 conduction bands, which were then utilized for the construction of the BSE Hamiltonian. The remaining conduction bands were compressed into 520 pseudobands, resulting in a total of 620 bands (including the 73 valence bands). The actual GW calculation was then conducted at the G_0W_0 level. For faster convergence of the G_0W_0 energies with respect to the k mesh, we used the nonuniform-neck-subsampling (NNS) technique [56]. As a substep, we calculated the static inverse dielectric function by employing a cutoff energy of 20 Ry for reciprocal lattice vectors and summing over 500 bands. Finally, we obtained the G_0W_0 energies of 27 valence and 27 conduction bands by summing again over 500 bands and using the same plane-wave cutoff as before. Then, for use in the ensuing BSE calculation, we recalculated the static inverse dielectric function applying the same settings as above, but without the NNS subsampling.

For solving the BSE, we considered 27 valence and 27 conduction bands in the construction of the direct and exchange kernel matrix. Note that for solving the BSE, we calculated wave functions on a finer k mesh, $10 \times 40 \times 1$, and interpolated the G_0W_0 corrections and the direct and exchange kernel to the finer grid (interpolating from the 27 coarse valence and 27 coarse conduction wave functions to 20 fine valence and 22 fine conduction wave functions). Then, by fully diagonalizing the BSE Hamiltonian, and employing the Tamm-Dancoff approximation,

$$\sum_{v'c'\boldsymbol{q}'} H_{vc\boldsymbol{q},v'c'\boldsymbol{q}'} X^m_{v'c'\boldsymbol{q}'} = \Omega_m X^m_{vc\boldsymbol{q}}, \tag{B4}$$

we obtained the exciton energies and eigenvectors for optical excitations, that is, excitations with center-of-mass momentum $\boldsymbol{Q} = 0$. As before, we utilized the BSE eigenvectors to construct the electron-hole wave functions

$$\Psi_m(\boldsymbol{r}_e, \boldsymbol{r}_h) = \sum_{vc} \sum_{\boldsymbol{q}}^{\mathrm{BZ}} X^m_{vc\boldsymbol{q}} \varphi^*_{v\boldsymbol{q}}(\boldsymbol{r}_h) \xi_{c\boldsymbol{q}}(\boldsymbol{r}_e). \tag{B5}$$

At this point, it is worth noting an important qualitative difference between the exciton wave function defined for the cluster in Eq. (B2) and the exciton wave function defined in Eq. (B5), which is due to the appearance of the Bloch wave functions $\varphi_{v\boldsymbol{q}}$ and $\xi_{c\boldsymbol{q}}$ in the latter. For a finite system in the presence of time-reversal symmetry, the orbitals and the BSE eigenvector entering Eq. (B2) are real valued, such that the cluster exciton wave function itself becomes a real-valued quantity. In contrast, in the periodic case, the orbitals are complex-valued Bloch waves, and also the BSE eigenvector is in general complex valued, such that the wave function of Eq. (B5) becomes complex. Only in cases where, in addition to time-reversal symmetry, also spatial inversion symmetry is present, does the $\boldsymbol{q} \to -\boldsymbol{q}$ symmetry lead to real-valued exciton wave functions. However, since 6T lacks an inversion center, the exciton wave function of Eq. (B5) is complex and nontrivial phases are to be expected. Note that the restriction to real-valued exciton wave functions in a cluster may pose a fundamental limitation for the determination of the internal phase structure of excitons, which is why, in addition to the cluster calculations, periodic calculations were performed and used as a basis for the exciton model presented in Appendix C and in the main text.

In the final step, we simulated photoemission angular distributions also for excitons in the periodic 6T layer, using the recently described exPOT formalism for periodic systems [57]. For zero center-of-mass momentum and omitting the $|\boldsymbol{A} \cdot \boldsymbol{k}|^2$ polarization factor, the photoemission intensity becomes

$$I_m(\boldsymbol{k}) \propto \sum_{v} \sum_{\boldsymbol{q}}^{\mathrm{BZ}} \left| \sum_{c} X^m_{vc\boldsymbol{q}} \mathcal{F}[\xi_{c\boldsymbol{q}}](\boldsymbol{k}) \right|^2 \cdot \delta(\omega + \Omega_m - \varepsilon_{v\boldsymbol{q}} - E_{\mathrm{kin}}). \tag{B6}$$

Note the additional sum over the Brillouin zone and the dependence on the Bloch vector $\boldsymbol{q}$ when comparing to the corresponding Eq. (B3) for nonperiodic clusters.

The so-obtained exciton wave function and momentum map for S_1 are shown in Figs. 3(b)–3(d). An analogous visualization of S_3 is given in Fig. 9. In both cases, the exciton wave function takes approximately the form of a combination of isolated molecule LUMOs located at different molecular sites [Fig. 9(a)]. A line cut of the exciton wave function exhibits maxima at each molecular site [Fig. 9(b)]. Fitting a Gaussian envelope function to

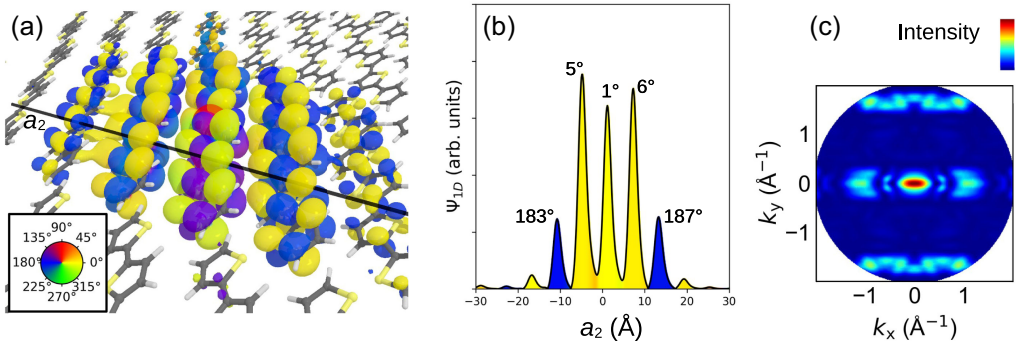

FIG. 9. In analogy to Fig. 3: (a) fixed-hole exciton wave function. (b) Line cut through the wave function along the a_2 line. (c) Momentum map calculated with Eq. (3) using the BSE eigenvector of S_3 instead of S_1.

these maxima, we extract a FWHM_x of approximately 16 Å for S_1, while we find approximately 20 Å to be fitting for S_3. Note that while these values serve as a rough estimate for the exciton delocalization, they should be taken with a grain of salt, since both S_1 and, especially, S_3, do not follow a perfect Gaussian, with, in particular, the central maximum being too low. It is noteworthy that the change of the complex phase between neighboring molecules is quite distinct between the two excitons: For S_1, we find a constant change of approximately 195° between neighboring molecules, while for S_3, the phase either changes by approximately 180° or approximately 0°. Figures 9(c) and 11(d) depict simulated momentum maps for S_1 and S_3, respectively. Their comparison clearly highlights the role of the phase in modulating the intensity in the momentum maps.

3. Comparison of cluster and periodic *ab initio* results

In this section, we compare key properties of the five systems for which we have performed GW and BSE calculations: (i) the monomer, (ii) the trimer, (iii) the tetramer, (iv) the hexamer, and (v) the periodic freestanding layer. The calculated optical absorption spectra for light polarized along the long molecular axis (y direction) are shown in Fig. 10. Note that each spectrum was normalized to a maximum value of 1.0 for better comparability. The monomer spectrum shows a single optically active exciton, while for the trimer and tetramer additional, albeit much weaker, optically active excitons appear. For the monolayer, we observe an overall redshift of the spectrum, which is due to the different computational treatment of the clusters as opposed to the extended monolayer. For the extended monolayer, we used a single-shot G_0W_0 calculation on top of a PBE starting point, while for the former we could afford B3LYP starting points and self-consistent *GW* corrections. The spectrum of the freestanding monolayer is dominated by two optically active excitons, where the first exciton S_1 exhibits a transition dipole moment about twice as large as the one of the next optically active exciton S_3. Finally, for the bilayer hexamer system, we observe an additional blueshift of the spectrum when compared to the other cluster calculations, which can be attributed to the changes in the electronic structure due to the now-present interlayer interaction. Importantly, it can be seen that the spectrum is composed of a multitude of optically active excited states with varying sizes of the transition dipole moment $|d_y|^2$. This complicates the simulation of excited-state photoemission, as detailed below.

The compositions of these optically active excitons are summarized in Table I, where the transition probability from valence orbital v to conduction orbital c in exciton m is given by

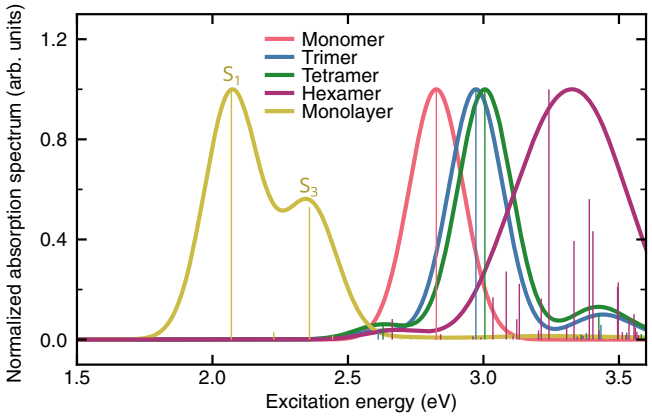

FIG. 10. The spectrum of the monomer is dominated by a single optically active exciton at 2.826 eV, which is also the lowest-energy excitation of the system. For the trimer (tetramer), the most active exciton is the third (fourth) one located at 2.972 eV (3.005 eV). In the monolayer, the lowest-energy exciton is located at 2.070 eV and is the most optically active one, followed by the third exciton which is located at 2.358 eV. In the hexamer (bilayer) system, the spectrum is composed of a multitude of optically active excitons with the overall most dominant one being located at 3.242 eV. Each vertical line denotes an individual (optically active) excited state, with the excited state's transition dipole moment $|d_y|^2$ determining the height of the line. The heights have been normalized on a per-system basis such that the brightest exciton of each system has a height of 1.0. Similarly, all spectra are normalized individually to a maximum value of 1.0.

TABLE I. Properties of low-lying dominant optically active excitons of the monomer, trimer, tetramer, monolayer, and hexamer. For each system, the transition dipole moment in the direction of the light polarization $|d_y|^2$ of the optically strongest exciton is normalized to 1. The last four columns contain the transition probabilities from HOMO (HOMO-1) to LUMO (LUMO+1) for each of the excitons. In addition to the excitation energy, the energy difference to the lowest excited state S_1 is given in parentheses.

System	Exciton	Excitation energy (eV)	$\lvert d_y\rvert^2$	H → L	H-1 → L + 1	H → L + 1	H-1 → L
Monomer	S_1	2.826	1.000	0.884	0.084	0.000	0.000
Trimer	S_3	2.972 (0.361)	1.000	0.882	0.066	0.007	0.009
Tetramer	S_4	3.005 (0.410)	1.000	0.883	0.062	0.008	0.010
Monolayer	S_1	2.070	1.000	0.931	0.031	0.006	0.008
Monolayer	S_3	2.358 (0.288)	0.529	0.916	0.021	0.025	0.017
Hexamer	S_{12}	3.084 (0.510)	0.272	0.948	0.014	0.023	0.004
Hexamer	S_{18}	3.242 (0.667)	1.000	0.932	0.017	0.021	0.013

$$p^m_{v\to c} = |X^m_{vc}|^2 \tag{B7}$$

in the cluster case and

$$p^m_{v\to c} = \sum_{\boldsymbol{q}}^{\mathrm{BZ}} |X^m_{vc\boldsymbol{q}}|^2 \tag{B8}$$

for the periodic monolayer. Specifically, we find that the contribution of the HOMO-1 to LUMO+1 transition shrinks from 8.4% in the monomer to 6.2% (6.6%) in the tetramer (trimer) and only 2%–3% in the monolayer. Conversely, going from the monolayer clusters to the full monolayer, the HOMO to LUMO transition grows even more in importance, fully dominating all other contributions to the excitons. For the hexamer system, we picked excitons 12 and 18 as exemplary excited states, since they are both rather low lying and optically bright. For both, we again find that they are dominated by the HOMO to LUMO transition, with the HOMO-1 to LUMO+1 transition contributing less than 2%. As a technical note regarding this analysis, we point out that, in the case of the many-molecule clusters, there are multiple orbitals with monomer-HOMO character and multiple orbitals with monomer-LUMO character. The same is true for all other monomer orbitals. Thus, when calculating the contribution of a particular transition to a given exciton, e.g., the HOMO to LUMO transition of the tetramer, we sum $p^m_{v\to c}$ over these orbitals. For the example of the HOMO to LUMO transition of the tetramer, this means that we sum up transitions across four valence and four conduction orbitals (making it a sum of 16 contributions).

Finally, we use the exPOT formalism to calculate photoemission momentum maps for all five systems. The results are shown in Fig. 11. A few points are noteworthy. First, the monomer does not exhibit the intensity modulation along the $k_y = 0$ line (Fig. 2(b)). Second, the intensity modulation already appears for the trimer (tetramer), however, with a smaller separation of the intensity peaks located at $k_{x,\mathrm{max}} \approx \pm 0.54$ Å^{-1} ($k_{x,\mathrm{max}} \approx \pm 0.54$ Å^{-1}) when compared to the experimental positions of $k_{x,\mathrm{max}} \approx \pm 0.85$ Å^{-1}. This value increases to $k_{x,\mathrm{max}} \approx \pm 0.64$ Å^{-1} in the case of S_1 of the monolayer system. Notably, the optically bright S_3 exciton of the monolayer [see Fig. 9(c)] also exhibits an intensity modulation along the $k_y = 0$ line. However, owing to the different phase modulation of the S_3 exciton wave function compared to the one of S_1, the intensity peak appears at the $\bar{\Gamma}$ point. Moreover, for S_1 and S_3 we observe slightly different intensity distributions in the minor-lobe region at $k_y \approx \pm 1.7$ Å^{-1}. However, because of the only approximately 0.3-eV higher excitation energy of S_3 and its weaker transition dipole moment compared to S_1 (see Fig. 10), the present time-resolved POT experiments are not able to reveal the presence of S_3.

For the hexamer cluster, S_{12} was chosen as an exemplary excited state as it is the lowest-lying exciton with appreciable oscillator strength. As can be seen from Fig. 11(e), it exhibits the same double-lobe momentum pattern along the $k_y = 0$ line. Note that the main absorption peak of the hexamer is composed of several excitons (see Fig. 10). From those, we expect the low-lying bright excitons S_{11} and S_{12} to correspond to the experimentally created excitation (see main text), both of which exhibit the characteristic double-lobe momentum pattern with only slightly varying $k_{x,\mathrm{max}}$ positions.

Finally we note that the exPOT formalism is also capable of simulating photoemission from optically dark states. Figure 12 shows the dark S_1 exciton of the tetramer system in comparison to the bright S_4 presented in Fig. 11(c). We observe that the dark exciton wave function of S_1 is more localized compared the bright S_4 state. Concomitantly, we find that the widths of two lobes in the corresponding

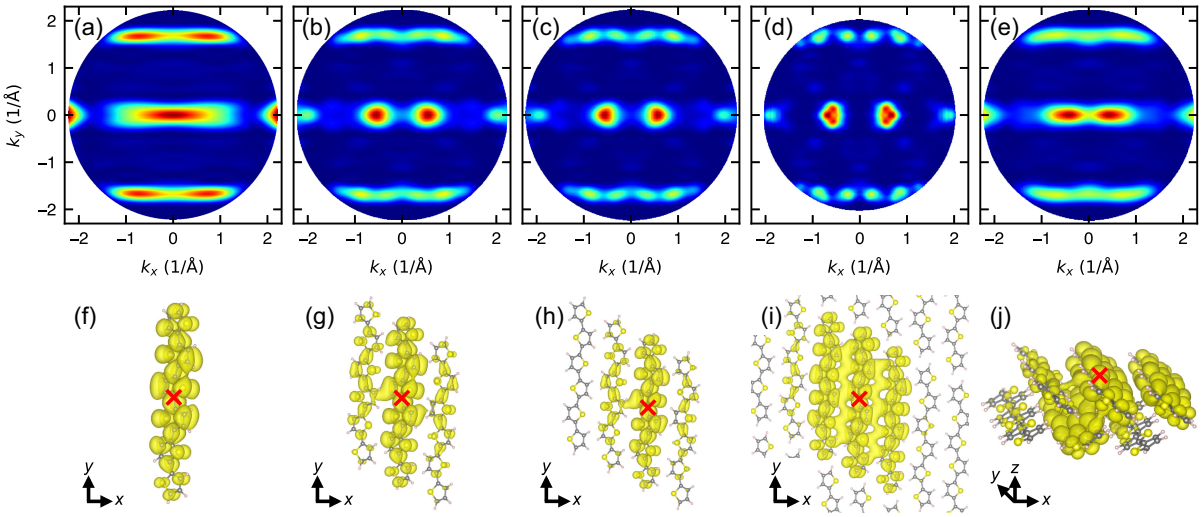

FIG. 11. (a) Simulated momentum map for S_1 of the monomer, (b) S_3 of the trimer, (c) S_4 of the tetramer, (d) S_1 of the monolayer, and (e) S_{12} of the hexamer. Panels (a)–(d) show emission from the dominant optically bright exciton of each system and show a clear progression toward an increase in the separation between the two intensity peaks along $k_y = 0$ (with the trimer and tetramer yielding practically the same separation). For the hexamer, panel (e), S_{12} is one of multiple low-lying bright excitons, as discussed in the text. Panels (f)–(j) show the corresponding fixed-hole electron density $|\Psi(\boldsymbol{r}_e, \boldsymbol{r}_h = \text{fixed})|^2$ (isosurface at 0.5% of maximum value). The hole has been fixed 0.5 Å above a carbon atom connecting the central thiophene rings, as indicated by the red crosses.

momentum map decrease, as expected, when comparing S_1 with S_4. Note that the maxima are at $k_{x,\max} \approx \pm 0.54$ Å^{-1} for both the bright and dark exciton, respectively, but FWHM_k shrinks from 0.53 Å^{-1} for S_1 to 0.43 Å^{-1} for S_4.

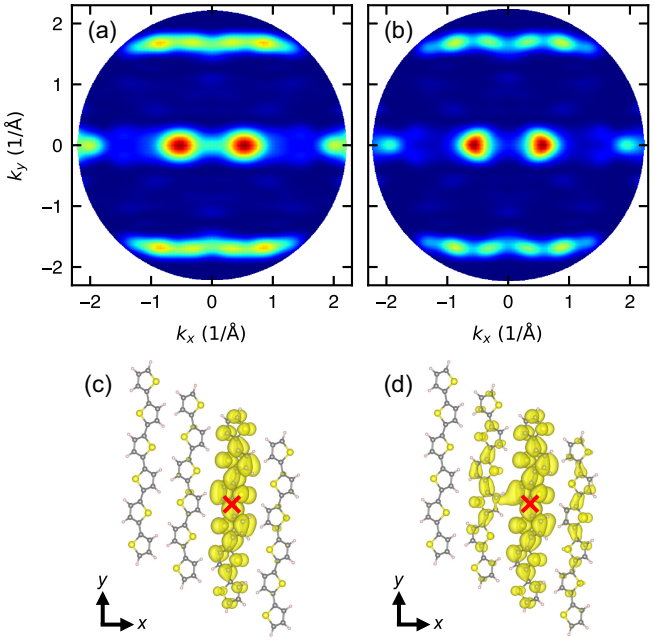

FIG. 12. (a) Simulated momentum map for S_1 of the tetramer and (b) S_4 of the tetramer. Panels (c) and (d) show the corresponding fixed-hole electron density $|\Psi(\boldsymbol{r}_e, \boldsymbol{r}_h = \text{fixed})|^2$ (isosurface at 0.5% of maximum value). The hole has been fixed 0.5 Å above a carbon atom connecting the central thiophene rings, as indicated by the red crosses.

APPENDIX C: RELATION OF THE EXCITON MODEL WITH FIRST-PRINCIPLES DESCRIPTION

1. exPOT formalism with Wannierized Dyson orbitals

The aim of this section is to show that the equation for the photoemission intensity from an excited state in a periodic system, derived in the plane-wave approximation and given in Ref. [57], can, in its most general form, be compactly written via localized Dyson orbitals, in close analogy to ground-state, nonperiodic POT (see, e.g., Eq. (10) in Ref. [58]).

To show this connection, we start from the general photoemission expression given in Ref. [57]

$$I_{m\boldsymbol{Q}}(\boldsymbol{k}) \propto |\boldsymbol{A}\cdot\boldsymbol{k}|^2 \sum_v \left| \sum_c X^{m\boldsymbol{Q}}_{vc\boldsymbol{q}} \mathcal{F}[\xi_{c\boldsymbol{q}+\boldsymbol{Q}}](\boldsymbol{q}+\boldsymbol{G}+\boldsymbol{Q}) \right|^2 \cdot \delta(\omega + \Omega_{m\boldsymbol{Q}} - \varepsilon_{v\boldsymbol{q}} - E_{\text{kin}}), \quad \text{with} \quad \boldsymbol{q}+\boldsymbol{G}+\boldsymbol{Q} = \boldsymbol{k}, \tag{C1}$$

which, in contrast to Eq. (B6), also allows for nonzero center-of-mass momentum $\boldsymbol{Q}$. Moreover, it explicitly includes the polarization factor, thus keeping the derivation as general as possible. Also note that in this formulation, the sum over $\boldsymbol{q}$ has been eliminated as explained in more detail in Ref. [57]. Briefly, we use the fact that

$$\mathcal{F}[\xi_{c\boldsymbol{q}+\boldsymbol{Q}}](\boldsymbol{k}) = \int_V \mathrm{d}^3 r \xi_{c\boldsymbol{q}+\boldsymbol{Q}}(\boldsymbol{r}) e^{-i\boldsymbol{k}\cdot\boldsymbol{r}} \tag{C2}$$

vanishes, unless $\boldsymbol{q}+\boldsymbol{G}+\boldsymbol{Q}=\boldsymbol{k}$ for at least one of the reciprocal lattice vectors $\boldsymbol{G}$. And since, for an arbitrary $\boldsymbol{k}$, this condition is either not fulfilled at all, or, at best, satisfied by a single $\boldsymbol{q}$ (and $\boldsymbol{G}$), we can drop the sum and restrict $\boldsymbol{k}$ to the $\boldsymbol{q}+\boldsymbol{G}+\boldsymbol{Q}$ grid spanned by the $\boldsymbol{Q}$ and $\boldsymbol{G}$ vectors.

We now use the above-described momentum conservation $\boldsymbol{q}+\boldsymbol{G}+\boldsymbol{Q}=\boldsymbol{k}$ to reintroduce a summation over $\boldsymbol{q}'$, which will ultimately allow us to introduce the concept of a Wannierized Dyson orbital as the central quantity of our photoemission formula. Because of the momentum conservation, we can write

$$\mathcal{F}[\xi_{c\boldsymbol{q}+\boldsymbol{Q}}](\boldsymbol{q}+\boldsymbol{G}+\boldsymbol{Q})=\sum_{\boldsymbol{q}'}^{\mathrm{BZ}}\mathcal{F}[\xi_{c\boldsymbol{q}'+\boldsymbol{Q}}](\boldsymbol{q}+\boldsymbol{G}+\boldsymbol{Q}), \tag{C3}$$

where only a single element in the summation contributes a nonzero value (namely, $\boldsymbol{q}'=\boldsymbol{q}$). Inserting this into Eq. (C1) and using the linearity of the Fourier transform, we find

$$\begin{aligned} I_{m\boldsymbol{Q}}(\boldsymbol{k}) \propto |\boldsymbol{A}\cdot\boldsymbol{k}|^2 \sum_v \left| \mathcal{F}\left[\sum_{\boldsymbol{q}'}^{\mathrm{BZ}}\sum_c X^{m\boldsymbol{Q}}_{vc\boldsymbol{q}'}\xi_{c\boldsymbol{q}'+\boldsymbol{Q}}\right](\boldsymbol{q}+\boldsymbol{G}+\boldsymbol{Q})\right|^2 \\ \cdot\delta(\omega+\Omega_{m\boldsymbol{Q}}-\varepsilon_{v\boldsymbol{q}}-E_{\mathrm{kin}}), \\ \text{with}\quad \boldsymbol{q}+\boldsymbol{G}+\boldsymbol{Q}=\boldsymbol{k}. \end{aligned} \tag{C4}$$

Next, we use the Dyson orbitals as defined in Ref. [57] as

$$D^{m\boldsymbol{Q}}_{v\boldsymbol{q}}(\boldsymbol{r})=\sum_c X^{m\boldsymbol{Q}}_{vc\boldsymbol{q}}\xi_{c\boldsymbol{q}+\boldsymbol{Q}}(\boldsymbol{r}) \tag{C5}$$

to observe that

$$\sum_{\boldsymbol{q}'}^{\mathrm{BZ}}\sum_c X^{m\boldsymbol{Q}}_{vc\boldsymbol{q}'}\xi_{c\boldsymbol{q}'+\boldsymbol{Q}}(\boldsymbol{r})=\sum_{\boldsymbol{q}'}^{\mathrm{BZ}} D^{m\boldsymbol{Q}}_{v\boldsymbol{q}'}(\boldsymbol{r}), \tag{C6}$$

which we insert into Eq. (C4) to get

$$\begin{aligned} I_{m\boldsymbol{Q}}(\boldsymbol{k}) \propto |\boldsymbol{A}\cdot\boldsymbol{k}|^2 \sum_v \left| \mathcal{F}\left[\sum_{\boldsymbol{q}'}^{\mathrm{BZ}} D^{m\boldsymbol{Q}}_{v\boldsymbol{q}'}\right](\boldsymbol{q}+\boldsymbol{G}+\boldsymbol{Q})\right|^2 \\ \cdot\delta(\omega+\Omega_{m\boldsymbol{Q}}-\varepsilon_{v\boldsymbol{q}}-E_{\mathrm{kin}}), \\ \text{with}\quad \boldsymbol{q}+\boldsymbol{G}+\boldsymbol{Q}=\boldsymbol{k}. \end{aligned} \tag{C7}$$

Finally, since in the Brillouin-zone summation only a single $\boldsymbol{q}'$ contributes [which of course does not mean that all but one of the Dyson orbitals $\{D^{m\boldsymbol{Q}}_{v\boldsymbol{q}'}(\boldsymbol{r})\}$ are zero valued, but rather, it simply means that only for one of them the Fourier transform is nonzero at position $\boldsymbol{q}+\boldsymbol{G}+\boldsymbol{Q}$, similar to what was detailed before in the context of Eq. (C3)] and since $|e^{-\mathrm{i}(\boldsymbol{q}'+\boldsymbol{Q})\cdot\boldsymbol{R}}|^2=1$ (where $\boldsymbol{R}$ is a lattice vector), we can write [which can also easily be verified by transforming Eq. (C8) back to Eq. (C7) while using the linearity of the Fourier transform]

$$I_{m\boldsymbol{Q}}(\boldsymbol{k}) \propto |\boldsymbol{A}\cdot\boldsymbol{k}|^2 \sum_v \left| \mathcal{F}\left[\frac{1}{\sqrt{N_{q'}}}\sum_{\boldsymbol{q}'}^{\mathrm{BZ}} e^{-\mathrm{i}(\boldsymbol{q}'+\boldsymbol{Q})\cdot\boldsymbol{R}} D^{m\boldsymbol{Q}}_{v\boldsymbol{q}'}\right](\boldsymbol{q}+\boldsymbol{G}+\boldsymbol{Q})\right|^2 \cdot\delta(\omega+\Omega_{m\boldsymbol{Q}}-\varepsilon_{v\boldsymbol{q}}-E_{\mathrm{kin}}), \quad \text{with}\quad \boldsymbol{q}+\boldsymbol{G}+\boldsymbol{Q}=\boldsymbol{k}, \tag{C8}$$

where $N_{q'}=N_q$ is the number of $\boldsymbol{q}$ vectors in the used mesh, i.e., the number of unit cells in the crystal, employing as usual Born–von Kármán periodic boundary conditions.

The expression inside the Fourier transform can be identified as a Wannierized Dyson orbital $D^{m\boldsymbol{Q}}_{v\boldsymbol{R}}$ at lattice site $\boldsymbol{R}$ [59]

$$\begin{aligned} D^{m\boldsymbol{Q}}_{v\boldsymbol{R}}(\boldsymbol{r}) &= \frac{1}{\sqrt{N_{q'}}}\sum_{\boldsymbol{q}'}^{\mathrm{BZ}} e^{-\mathrm{i}(\boldsymbol{q}'+\boldsymbol{Q})\cdot\boldsymbol{R}} D^{m\boldsymbol{Q}}_{v\boldsymbol{q}'}(\boldsymbol{r}) \\ &= \frac{1}{\sqrt{N_{q'}}}\sum_{\boldsymbol{q}'}^{\mathrm{BZ}}\sum_c e^{-\mathrm{i}(\boldsymbol{q}'+\boldsymbol{Q})\cdot\boldsymbol{R}} X^{m\boldsymbol{Q}}_{vc\boldsymbol{q}'}\xi_{c\boldsymbol{q}'+\boldsymbol{Q}}(\boldsymbol{r}), \end{aligned} \tag{C9}$$

allowing us to write

$$\begin{aligned} I_{m\boldsymbol{Q}}(\boldsymbol{k}) \propto |\boldsymbol{A}\cdot\boldsymbol{k}|^2 \sum_v |\mathcal{F}[D^{m\boldsymbol{Q}}_{v\boldsymbol{R}}](\boldsymbol{q}+\boldsymbol{G}+\boldsymbol{Q})|^2 \\ \cdot\delta(\omega+\Omega_{m\boldsymbol{Q}}-\varepsilon_{v\boldsymbol{q}}-E_{\mathrm{kin}}), \\ \text{with}\quad \boldsymbol{q}+\boldsymbol{G}+\boldsymbol{Q}=\boldsymbol{k}. \end{aligned} \tag{C10}$$

Based on this final expression, we can interpret photoemission from an excited state as resulting from a sum over the valence bands of the system, where each band contributes via the Fourier transform of a Wannier-Dyson orbital (built from conduction-band wave functions) modulated by a band-structure-dependent energy-conserving function. The advantage of this particular formulation is that the use of a Wannier-Dyson orbital naturally reflects the localized character of the excited state, which makes its

further analysis particularly lucid, similar to a recently proposed scheme [60]. We also note that the photoemission expression Eq. (C10) is independent of the position $\boldsymbol{R}$ of the Wannier-Dyson orbital, reflecting the periodic nature of the crystal.

Having this new formulation at hand, we can now apply it to the special case of the 6T monolayer excitons S_1 and S_3 discussed above. These excitons have a center-of-mass momentum $\boldsymbol{Q} = 0$ and are, to a good approximation, comprised of only transitions between the HOMO band and LUMO band (see Table I). Dropping the polarization factor for simplicity and choosing $\boldsymbol{R} = 0$ (since the position of the Wannier-Dyson orbital does not matter, as shown above), Eq. (C10) becomes

$$I_m(\boldsymbol{k}) \propto |\mathcal{F}[D^m_{v_1\boldsymbol{R}=0}](\boldsymbol{q}+\boldsymbol{G})|^2 \cdot \delta(\omega + \Omega_m - \varepsilon_{v_1\boldsymbol{q}} - E_{\mathrm{kin}}), \quad \text{with} \quad \boldsymbol{q}+\boldsymbol{G}=\boldsymbol{k}. \tag{C11}$$

Additionally, in order to mimic the finite kinetic-energy integration window used to obtain experimental momentum maps, we integrate Eq. (C11) over the kinetic energy. To calculate a kinetic-energy-integrated momentum map, we integrate over k_z at each position (k_x, k_y),

$$I_m(k_x,k_y) \propto \int_0^\infty d_{k_z} |\mathcal{F}[D^m_{v_1\boldsymbol{R}=0}](\boldsymbol{q}+\boldsymbol{G})|^2 \cdot \delta\left(\omega + \Omega_m - \varepsilon_{v_1\boldsymbol{q}} - \frac{1}{2}(k_x^2+k_y^2+k_z^2)\right), \quad \text{with} \quad \boldsymbol{q}+\boldsymbol{G}=\boldsymbol{k}. \tag{C12}$$

Note that when integrating over k_z from 0 to ∞, we integrate over all kinetic energies at which photoemission occurs. For the present system of a 6T monolayer and photoemission from the HOMO band, this is justified because the band was found to have a very small bandwidth of less than 0.1 eV. Note also that for more dispersive valence bands, especially when the band dispersion is larger than the energy integration window used in experiment, this approach is not viable, and the integration should instead be formulated in terms of kinetic energies and performed over a finite-energy window. Continuing now with the energy integration, since $q_z = 0$ (as usual, our repeated-slab calculation does not sample the q_z direction) and q_x and q_y are fixed at each (k_x, k_y) by $\boldsymbol{q}+\boldsymbol{G}=\boldsymbol{k}$, inside the integral for a given (k_x, k_y) we find $\boldsymbol{q}$ to be a constant vector and $\varepsilon_{v_1\boldsymbol{q}}$ a constant number. Therefore, also $\omega + \Omega_m - \varepsilon_{v_1\boldsymbol{q}}$ is a constant and the delta function is satisfied only for a single value of k_z, namely,

$$k_z = \sqrt{2(\omega + \Omega_m - \varepsilon_{v_1\boldsymbol{q}}) - k_x^2 - k_y^2}. \tag{C13}$$

Thus, we finally obtain the kinetic-energy-integrated photoemission expression

$$I_m(k_x,k_y) \propto |\mathcal{F}[D^m_{v_1\boldsymbol{R}=0}](\boldsymbol{q}+\boldsymbol{G})|^2, \quad \text{with} \quad q_x+G_x=k_x, \quad q_y+G_y=k_y, \quad \text{and} \quad q_z=0, \quad G_z=\sqrt{2(\omega+\Omega_m-\varepsilon_{v_1\boldsymbol{q}})-k_x^2-k_y^2}. \tag{C14}$$

Note that in the case of a flat HOMO band $\varepsilon_{v_1\boldsymbol{q}} = \varepsilon_{v_1}$, this result trivially equates to simply using Eq. (C11) at the $\boldsymbol{k}$ vectors satisfying $E_{\mathrm{kin}} = \frac{1}{2}|\boldsymbol{k}|^2 = \omega + \Omega_m - \varepsilon_{v_1}$, with the delta function being effectively set to 1. Ensuring a sufficiently large vacuum slab in the repeated-slab geometry, the spacing of reciprocal lattice vectors $\boldsymbol{G}$ in the k_z direction becomes fine enough, such that the condition on G_z can be well met. To avoid overly lengthy formulas during the rest of this section, we compactly write Eq. (C14) as

$$I_m(\boldsymbol{k}) \propto |\mathcal{F}[D^m_{v_1\boldsymbol{R}=0}](\boldsymbol{q}+\boldsymbol{G})|^2, \quad \text{with} \quad \boldsymbol{q}+\boldsymbol{G}=\boldsymbol{k}. \tag{C15}$$

Note therefore that whenever Eq. (C15) is referenced, Eq. (C14) represents its formally correct counterpart as the kinetic-energy-integrated photoemission intensity. Similarly, all upcoming equations derived from Eq. (C15) are to be understood as compact versions of their formally correct counterparts analogous to Eq. (C14).

Based on Eq. (C15), the photoemission intensity is simply the absolute square of a single Fourier-transformed Dyson orbital, which itself is, according to Eq. (C9), composed of LUMO band Bloch functions

$$D^m_{v_1\boldsymbol{R}=0}(\boldsymbol{r}) = \frac{1}{\sqrt{N_q}} \sum_{\boldsymbol{q}}^{\mathrm{BZ}} X^m_{v_1c_1\boldsymbol{q}} \xi_{c_1\boldsymbol{q}}(\boldsymbol{r}). \tag{C16}$$

2. Derivation of the exciton model as a Wannierized Dyson orbital

By creating a model that emulates the Dyson orbital, Eq. (C16), we can directly simulate the photoemission process based on an easy-to-understand model function, without the need for expensive calculations. To arrive at the model Eq. (1) used in the main text, we first note that, by Wannierizing the LUMO band Bloch functions as

$$\xi_{c_1\boldsymbol{R}'}(\boldsymbol{r}) = \frac{1}{\sqrt{N_q}} \sum_{\boldsymbol{q}}^{\mathrm{BZ}} e^{-i\boldsymbol{q}\cdot\boldsymbol{R}'} \xi_{c_1\boldsymbol{q}}(\boldsymbol{r}), \tag{C17}$$

we can also write the Dyson orbital as a linear combination of localized functions, which span the same space as the Bloch functions

$$D^m_{v_1\boldsymbol{R}=0}(\boldsymbol{r}) = \sum_{\boldsymbol{R}'}^{\mathrm{crystal}} c^m_{v_1\boldsymbol{R}'} \xi_{c_1\boldsymbol{R}'}(\boldsymbol{r}), \tag{C18}$$

where the coefficients $c^m_{v_1\boldsymbol{R}'}$ are connected to the BSE eigenvector via the inverse Fourier transform (multiplied by an additional $1/\sqrt{N_q}$ factor)

$$c^m_{v_1\boldsymbol{R}'} = \frac{1}{N_q}\sum_{\boldsymbol{q}}^{\mathrm{BZ}} X^m_{v_1c_1\boldsymbol{q}} e^{i\boldsymbol{q}\cdot\boldsymbol{R}'}. \tag{C19}$$

Next, we approximate the generic coefficients $c^m_{v_1\boldsymbol{R}'}$ in Eq. (C18) by the product of a real-valued envelope function $\alpha(\boldsymbol{R})$ controlling the extent of the Dyson orbital, and a site-dependent complex phase factor $e^{i\beta(\boldsymbol{R})}$. Finally, we approximate the Wannierized LUMO functions $\xi_{c_1\boldsymbol{R}'}$ in Eq. (C18) by the LUMO of an isolated, single-molecule calculation ξ_L placed at the lattice sites $\boldsymbol{R}'$ and arrive at the model [Eq. (1) in the main text]

$$D^m_{v_1\boldsymbol{R}=0}(\boldsymbol{r}) = \sum_{\boldsymbol{R}'}^{\mathrm{crystal}} \alpha(\boldsymbol{R}')e^{i\beta(\boldsymbol{R}')}\xi_L(\boldsymbol{r}-\boldsymbol{R}'). \tag{C20}$$

Via the connection Eq. (C19) (see also Figs. 13(b), 13(f), 14(b), and 14(f)] between the BSE eigenvector and the model coefficients, it becomes clear that we can use our model wave function to not only simulate photoemission from an excited state, but we can also employ it to gain an understanding of the structure of excited states [e.g., by fitting the model to experimental data and using Eq. (C19) to construct the exciton wave function]. Conversely, we can use the exciton wave function from an *ab initio* calculation to motivate a model choice (α and β), which can then be used for systems or excitations, where the *ab initio* data may not be available. For the present case of a 6T monolayer, using a Gaussian envelope function α proved successful. For β, we propose two choices: (i) Setting $e^{i\beta(\boldsymbol{R})} = e^{i\boldsymbol{q}\boldsymbol{R}}$, the phase changes periodically across the surface, leading to a constant phase difference between neighboring molecules. This resembles exactly the situation found in S_1, where the phase difference between neighboring molecules was found to be approximately 195°; see Fig. 3(c). (ii) Allowing $\beta(\boldsymbol{R})$ to be only 0 or π, we get $e^{i\beta(\boldsymbol{R})} = \pm 1$. At each molecular site, the value of β may be chosen individually, such that two neighbors may either have equal phases, or a phase difference of π. This structure is found in S_3 [see Fig. 9(b)], and to some approximation also works for modeling S_1 (since 195° is not too far from a phase change of π). Based on the π-orbital structure of the LUMO wave function, this model choice can be understood as a combination of antibonding (no phase change) and bonding (phase change of π) overlaps, as can be seen in Figs. 3(b) and 9(a).

As shown in Eq. (C15), the photoemission intensity for S_1 and S_3 of the 6T monolayer system is simply the absolute square of a Fourier-transformed Wannier-Dyson

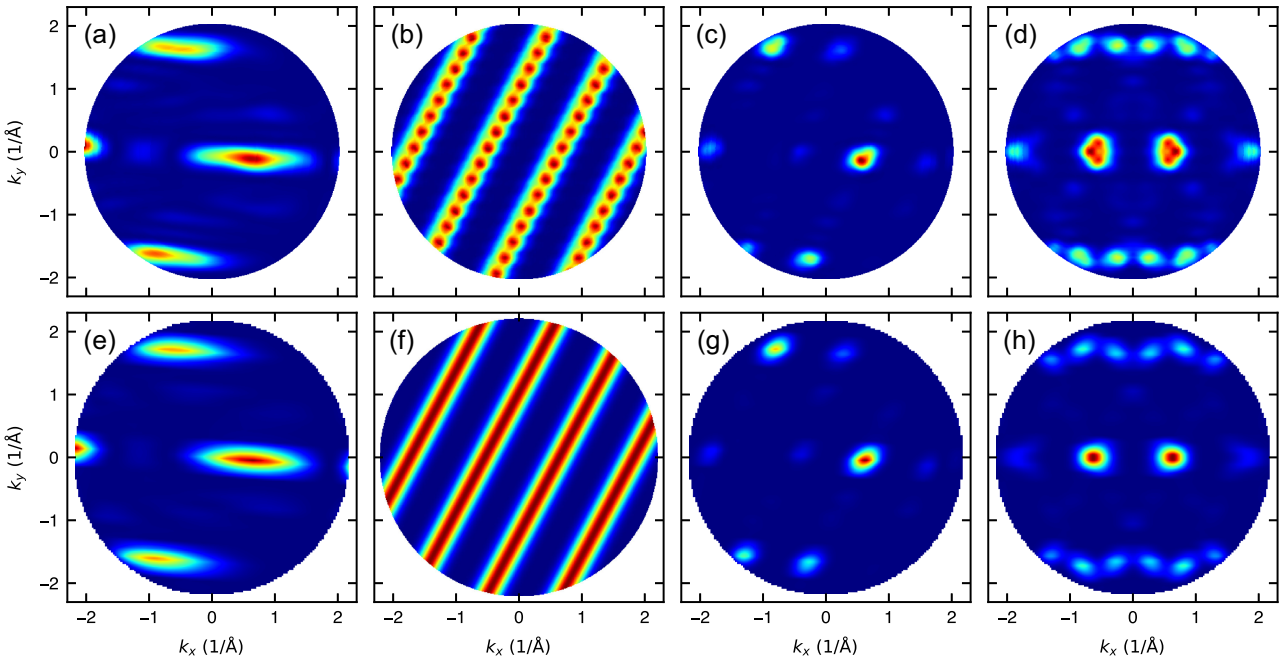

FIG. 13. (a)–(d) Decomposition of the photoemission intensity of exciton S_1 from the *ab initio* exPOT simulation into individual contributions. (a) Absolute square of the Fourier-transformed LUMO band wave functions $|\mathcal{F}[\xi_{c_1\boldsymbol{q}}](\boldsymbol{q}+\boldsymbol{G})|^2$. (b) Absolute square of the BSE eigenvector $|X^m_{v_1c_1\boldsymbol{q}}|^2$ from Eq. (C23). Panel (d) shows the symmetrized photoemission intensity shown in panel (c). (e)–(h) Analogous to (a)–(d) but for the exciton model following Eq. (C21). (e) Absolute square of a Fourier-transformed LUMO of a gas-phase molecule $|\mathcal{F}[\xi_L](\boldsymbol{k})|^2$. (f) Factor $|\sum_{\boldsymbol{R}}^{\mathrm{crystal}} \alpha(\boldsymbol{R})e^{i\beta(\boldsymbol{R})}e^{-i\boldsymbol{k}\cdot\boldsymbol{R}}|^2$ arising from the envelope function and model phase factor. Panel (g) and (h) show the photoemission intensity $I_{\mathrm{model}}(\boldsymbol{k})$ [product of panels (e) and (f)], before and after symmetrization, respectively.

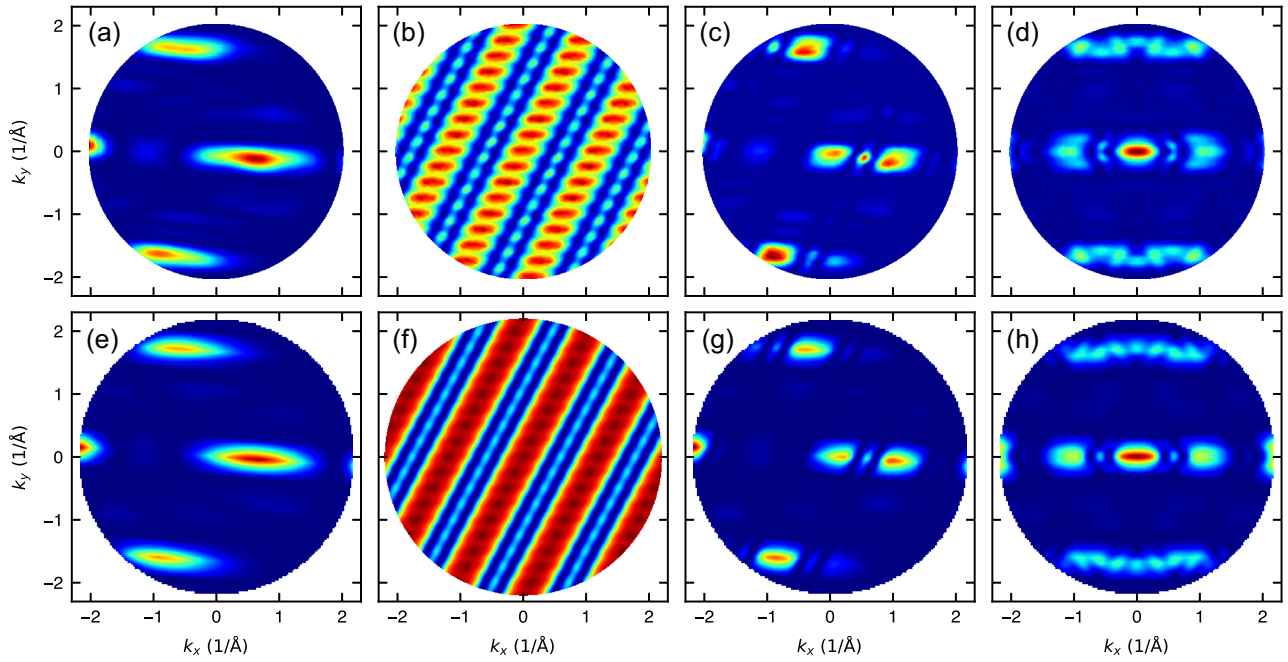

FIG. 14. Analogous to Fig. 13 but for exciton S_3, the first row shows *ab initio* photoemission as calculated with Eq. (C23), while the second row shows photoemission using the model Eq. (C20) and is thus based on Eq. (C21).

orbital. Using our model function Eq. (C20) for the Wannier-Dyson orbital, we thus find

$$I_{\text{model}}(\boldsymbol{k}) \propto \left| \sum_{\boldsymbol{R}}^{\text{crystal}} \alpha(\boldsymbol{R}) e^{\mathrm{i}\beta(\boldsymbol{R})} e^{-\mathrm{i}\boldsymbol{k}\cdot\boldsymbol{R}} \right|^2 \cdot |\mathcal{F}[\xi_L](\boldsymbol{k})|^2. \quad \text{(C21)}$$

This equation corresponds to Eq. (2) in the main text. As is shown in Appendix C 3 below, this simple form of the photoemission intensity as a product of two terms allows for direct insights into the origin of fine details found in momentum maps.

To summarize a lengthy derivation, we have thus shown that the model used to analyze our experimental data can be derived from the accurate equations of the exPOT formalism.

For comparability, we conclude this section by bringing the *ab initio* photoemission expression Eq. (C15) to a form similar to the model expression Eq. (C21). First, we insert Eq. (C16) into Eq. (C15) to get

$$I_m(\boldsymbol{k}) \propto \left| \mathcal{F}\left[\sum_{\boldsymbol{q}'}^{\text{BZ}} X^m_{v_1 c_1 \boldsymbol{q}'} \xi_{c_1 \boldsymbol{q}'} \right](\boldsymbol{q}+\boldsymbol{G}) \right|^2, \quad \text{with} \quad \boldsymbol{q}+\boldsymbol{G}=\boldsymbol{k}. \quad \text{(C22)}$$

Then, we use the linearity of the Fourier transform and momentum conservation [see text below Eq. (C2)] to arrive at the final expression [Eq. (3) in the main text]

$$I_m(\boldsymbol{k}) \propto |X^m_{v_1 c_1 \boldsymbol{q}}|^2 \cdot |\mathcal{F}[\xi_{c_1 \boldsymbol{q}}](\boldsymbol{q}+\boldsymbol{G})|^2, \quad \text{with} \quad \boldsymbol{q}+\boldsymbol{G}=\boldsymbol{k}. \quad \text{(C23)}$$

3. Comparison of photoemission from *ab initio* calculations and the exciton model

The similar form of the model photoemission expression Eq. (C21) and the *ab initio* expression Eq. (C23) invites a direct comparison of the two approaches. To start, Fig. 13 shows a comparison of a photoemission map of S_1 from the monolayer *ab initio* calculation [Figs. 13(a)–13(d)], with the corresponding photoemission simulation based on the model depicted in Figs. 13(e)–13(h).

For the *ab initio* simulation, based on Eq. (C23), we can simply calculate the photoemission intensity $I_m(\boldsymbol{k})$ [Fig. 13(c)] as the product of the LUMO band photoemission map $|\mathcal{F}[\xi_{c_1\boldsymbol{q}}](\boldsymbol{q}+\boldsymbol{G})|^2$ [Fig. 13(a)] and the BSE eigenvector $|X^m_{v_1 c_1 \boldsymbol{q}}|^2$ [Fig. 13(b)]. We note that the LUMO band map trivially shows the tilt [Fig. 8(b)] and the small misalignment of the long molecular axis with respect to the a_1 axis [Fig. 8(a)] of the monolayer geometry. Also note that the BSE eigenvector exhibits a stripelike structure, with the angle of the stripes being determined by the unit-cell slip; see Fig. 8. Figure 8(d) shows the symmetrized [for 6T molecules on the Cu(110)-(2×1)O substrate] photoemission intensity exhibiting the now well-known double peak along the $k_y = 0$ line.

In comparison, the second row of Fig. 13 shows the photoemission intensity calculated for the model wave

function Eq. (C20), that is, based on Eq. (C21). For the LUMO wave function ξ_L ($|\mathcal{F}[\xi_L](\boldsymbol{k})|^2$ in Fig. 13(e), we use the LUMO from a DFT calculation of an isolated 6T molecule and rotate it in accordance with the monolayer geometry. Figure 13(f) shows the first factor on the right-hand side of Eq. (C21) $|\sum_{\boldsymbol{R}}^{\text{crystal}} \alpha(\boldsymbol{R}) e^{i\beta(\boldsymbol{R})} e^{-i\mathbf{k}\cdot\boldsymbol{R}}|^2$, and is thus determined by the envelope function and phase factor used in the model. The molecular sites $\boldsymbol{R}$ are taken from the monolayer geometry, and we use a Gaussian envelope function α with a FWHM_x of 13 Å, in reasonable agreement with the estimate of 16 Å given above, and phase factors $e^{i\beta(\boldsymbol{R})}$ corresponding to a 195° phase change between neighboring molecules (in the $\mathbf{a_2}$ direction). The resulting factor then shows the same stripelike nature as the BSE eigenvector, making the above-shown link, Eq. (C19), between the two quantities obvious. Finally, Figs. 13(g) and 13(h) again show the unsymmetrized and symmetrized photoemission intensities $I_{\text{model}}(\boldsymbol{k})$, respectively. Again, comparison to the *ab initio* simulations in Figs. 13(c) and 13(d) shows great resemblance, demonstrating the strength of the model, allowing us to understand most of the details of S_1 in terms of just the used FWHM_x and phase change.

Similarly, Fig. 14 shows the photoemission from S_3, with the first row again showing the *ab initio* exPOT result and the second row showing photoemission based on the model. For the model, we use a Gaussian envelope function α with a FWHM_x of 18 Å, which is again in good agreement with the 19.9-Å estimate given before, and assign phase factors $e^{i\beta(\boldsymbol{R})} = \pm 1$ based on Fig. 9(b). Comparing Figs. 14(b) and 14(f), we can see that the model reproduces both the major and minor stripes of the BSE eigenvector. This leads to very good agreement of the symmetrized photoemission intensities shown in Figs. 14(d) and 14(h), where also the minor-lobe structure agrees very well. Thus, the excited-state photoemission can be reproduced to high accuracy by the model Eq. (C20), and can therefore be understood via a combination of bonding and antibonding LUMO wave functions weighted by a Gaussian envelope function.

[1] F. C. Spano, *Excitons in Conjugated oligomer aggregates, films, and crystals*, Annu. Rev. Phys. Chem. **57**, 217 (2006).

[2] A. Köhler and H. Bässler, *Electronic Processes in Organic Semiconductors* (Wiley-VCH, New York, 2015).

[3] H. Bronstein, Z. Chen, R. S. Ashraf, W. Zhang, J. Du, J. R. Durrant, P. Shakya Tuladhar, K. Song, S. E. Watkins, Y. Geerts, M. M. Wienk, R. A. J. Janssen, T. Anthopoulos, H. Sirringhaus, M. Heeney, and I. McCulloch, *Thieno[3,2-b] thiophene-diketopyrrolopyrrole-containing polymers for high-performance organic field-effect transistors and organic photovoltaic devices*, J. Am. Chem. Soc. **133**, 3272 (2011).

[4] T. R. Nelson, D. Ondarse-Alvarez, N. Oldani, B. Rodriguez-Hernandez, L. Alfonso-Hernandez, J. F. Galindo, V. D. Kleiman, S. Fernandez-Alberti, A. E. Roitberg, and S. Tretiak, *Coherent exciton-vibrational dynamics and energy transfer in conjugated organics*, Nat. Commun. **9**, 2316 (2018).

[5] A. J. Sneyd *et al.*, *Efficient energy transport in an organic semiconductor mediated by transient exciton delocalization*, Sci. Adv. **7**, eabh4232 (2021).

[6] G. D. Scholes, *A molecular perspective on quantum information*, Proc. R. Soc. A **479**, 20230599 (2023).

[7] Y. Zhang, C. P. Oberg, Y. Hu, H. Xu, M. Yan, G. D. Scholes, and M. Wang, *Molecular and supramolecular materials: From light-harvesting to quantum information science and technology*, J. Phys. Chem. Lett. **15**, 3294 (2024).

[8] A. Yamauchi, K. Tanaka, M. Fuki, S. Fujiwara, N. Kimizuka, T. Ryu, M. Saigo, K. Onda, R. Kusumoto, N. Ueno, H. Sato, Y. Kobori, K. Miyata, and N. Yanai, *Room-temperature quantum coherence of entangled multiexcitons in a metal-organic framework*, Sci. Adv. **10**, eadi3147 (2024).

[9] R. Wallauer, M. Raths, K. Stallberg, L. Münster, D. Brandstetter, X. Yang, J. Güdde, P. Puschnig, S. Soubatch, C. Kumpf, F. C. Bocquet, F. S. Tautz, and U. Höfer, *Tracing orbital images on ultrafast time scales*, Science **371**, 1056 (2021).

[10] A. Neef, S. Beaulieu, S. Hammer, S. Dong, J. Maklar, T. Pincelli, R. P. Xian, M. Wolf, L. Rettig, J. Pflaum, and R. Ernstorfer, *Orbital-resolved observation of singlet fission*, Nature (London) **616**, 275 (2023).

[11] W. Bennecke, A. Windischbacher, D. Schmitt, J. P. Bange, R. Hemm, C. S. Kern, G. D'Avino, X. Blase, D. Steil, S. Steil, M. Aeschlimann, B. Stadtmüller, M. Reutzel, P. Puschnig, G. S. M. Jansen, and S. Mathias, *Disentangling the multiorbital contributions of excitons by photoemission exciton tomography*, Nat. Commun. **15**, 1804 (2024).

[12] W. Bennecke, I. Gonzalez Oliva, J. P. Bange, P. Werner, D. Schmitt, M. Merboldt, A. M. Seiler, K. Watanabe, T. Taniguchi, D. Steil, R. T. Weitz, P. Puschnig, C. Draxl, G. S. M. Jansen, M. Reutzel, and S. Mathias, *Hybrid Frenkel-Wannier excitons facilitate ultrafast energy transfer at a 2D-organic interface*, Nat. Phys. **21**, 1973 (2025).

[13] S. Dong, M. Puppin, T. Pincelli, S. Beaulieu, D. Christiansen, H. Hübener, C. W. Nicholson, R. P. Xian, M. Dendzik, Y. Deng, Y. W. Windsor, M. Selig, E. Malic, A. Rubio, A. Knorr, M. Wolf, L. Rettig, and R. Ernstorfer, *Direct measurement of key exciton properties: Energy, dynamics, and spatial distribution of the wave function*, Nat. Sci. **1**, e10010 (2021).

[14] M. K. L. Man, J. Madeo, C. Sahoo, K. Xie, M. Campbell, V. Pareek, A. Karmakar, E. L. Wong, A. Al-Mahboob, N. S. Chan, D. R. Bacon, X. Zhu, M. M. M. Abdelrasoul, X. Li, T. F. Heinz, F. H. da Jornada, T. Cao, and K. M. Dani, *Experimental measurement of the intrinsic excitonic wave function*, Sci. Adv. **7**, eabg0192 (2021).

[15] D. Schmitt, J. P. Bange, W. Bennecke, A. AlMutairi, G. Meneghini, K. Watanabe, T. Taniguchi, D. Steil, D. R. Luke, R. T. Weitz, S. Steil, G. S. M. Jansen, S. Brem, E. Malic, S. Hofmann, M. Reutzel, and S. Mathias, *Formation of moiré*

interlayer excitons in space and time, Nature (London) **608**, 499 (2022).

[16] O. Karni *et al.*, *Structure of the moiré exciton captured by imaging its electron and hole*, Nature (London) **603**, 247 (2022).

[17] K. Mourzidis, V. Jindal, M. Glazov, A. Balocchi, C. Robert, D. Lagarde, P. Renucci, L. Lombez, T. Taniguchi, K. Watanabe, T. Amand, S. Francoeur, and X. Marie, *Exciton formation in two-dimensional semiconductors*, Phys. Rev. X **15**, 031078 (2025).

[18] S. Roux *et al.*, *Exciton self-trapping in twisted hexagonal boron nitride homostructures*, Phys. Rev. X **15**, 021067 (2025).

[19] Y. Dong, V. C. Nikolis, F. Talnack, Y.-C. Chin, J. Benduhn, G. Londi, J. Kublitski, X. Zheng, S. C. B. Mannsfeld, D. Spoltore, L. Muccioli, J. Li, X. Blase, D. Beljonne, J.-S. Kim, A. A. Bakulin, G. D'Avino, J. R. Durrant, and K. Vandewal, *Orientation dependent molecular electrostatics drives efficient charge generation in homojunction organic solar cells*, Nat. Commun. **11**, 4617 (2020).

[20] S. Frolov, C. Kloc, S. Berg, G. Thomas, and B. Batlogg, *Transient spectroscopy of Frenkel excitons in α-hexathiophene single crystals*, Chem. Phys. Lett. **326**, 558 (2000).

[21] F. Kouki, P. Spearman, P. Valat, G. Horowitz, and F. Garnier, *Experimental determination of excitonic levels in α-oligothiophenes*, J. Chem. Phys. **113**, 385 (2000).

[22] E. Varene, L. Bogner, C. Bronner, and P. Tegeder, *Ultrafast exciton population, relaxation, and decay dynamics in thin oligothiophene films*, Phys. Rev. Lett. **109**, 207601 (2012).

[23] W. Bronsch, T. Wagner, S. Baum, M. Wansleben, K. Zielke, E. Ghanbari, M. Györök, A. Navarro-Quezada, P. Zeppenfeld, M. Weinelt, and C. Gahl, *Interplay between morphology and electronic structure in α-Sexithiophene films on* Au(111), J. Phys. Chem. C **123**, 7931 (2019).

[24] J.-W. van der Horst, P. A. Bobbert, M. A. J. Michels, G. Brocks, and P. J. Kelly, *Ab Initio calculation of the electronic and optical excitations in polythiophene: Effects of intra- and interchain screening*, Phys. Rev. Lett. **83**, 4413 (1999).

[25] G. Bussi, A. Ruini, E. Molinari, M. J. Caldas, P. Puschnig, and C. Ambrosch-Draxl, *Interchain interaction and Davydov splitting in polythiophene crystals: An ab initio approach*, Appl. Phys. Lett. **80**, 4118 (2002).

[26] X. Leng, H. Yin, D. Liang, and Y. Ma, *Excitons and Davydov splitting in sexithiophene from first-principles many-body Green's function theory*, J. Chem. Phys. **143**, 114501 (2015).

[27] L. Sun, S. Berkebile, G. Weidlinger, M. Denk, R. Denk, M. Hohage, G. Koller, F. P. Netzer, M. G. Ramsey, and P. Zeppenfeld, *Layer resolved evolution of the optical properties of α-sexithiophene thin films*, Phys. Chem. Chem. Phys. **14**, 13651 (2012).

[28] S. Berkebile, G. Koller, P. Puschnig, C. Ambrosch-Draxl, F. P. Netzer, and M. G. Ramsey, *Angle-resolved photoemission of chain-like molecules: the electronic band structure of sexithiophene and sexiphenyl*, Appl. Phys. A **95**, 101 (2009).

[29] M. Stettner, S. Kaidisch, A. V. Matetskiy, E. Fackelman, S. Soubatch, C. Kumpf, F. C. Bocquet, M. G. Ramsey, P. Puschnig, and F. S. Tautz, *Tracing the film structure of an organic semiconductor with photoemission orbital tomography*, arXiv:2603.06204.

[30] T. Chowdhury, A. Champagne, P. Knüppel, Z. Naqvi, A. Ray, M. Gao, D. A. Muller, N. Guisinger, K. F. Mak, J. B. Neaton, and J. Park, *Bright hybrid excitons in molecularly tunable bilayer crystals*, arXiv:2502.13460.

[31] G. Horowitz, B. Bachet, A. Yasser, P. Lang, F. Demanze, J.-L. Fave, and F. Garnier, *Growth and Characterization of Sexithiophene Single Crystals*, Chem. Mater. **7**, 1337 (1995).

[32] C. Cocchi and C. Draxl, *Optical spectra from molecules to crystals: Insight from many-body perturbation theory*, Phys. Rev. B **92**, 205126 (2015).

[33] C. S. Kern, A. Windischbacher, and P. Puschnig, *Photoemission orbital tomography for excitons in organic molecules*, Phys. Rev. B **108**, 085132 (2023).

[34] P. Puschnig, S. Berkebile, A. J. Fleming, G. Koller, K. Emtsev, T. Seyller, J. D. Riley, C. Ambrosch-Draxl, F. P. Netzer, and M. G. Ramsey, *Reconstruction of molecular orbital densities from photoemission data*, Science **326**, 702 (2009).

[35] M. Theilen, S. Kaidisch, M. Stettner, S. Zajusch, E. Fackelman, A. Adamkiewicz, R. Wallauer, A. Windischbacher, C. S. Kern, M. G. Ramsey, F. C. Bocquet, S. Soubatch, F. S. Tautz, U. Höfer, and P. Puschnig, *Data Repository, Jülich DATA*, 10.26165/JUELICH-DATA/HEKKRZ, (2026).

[36] S. Kishimoto, M. Kageshima, Y. Naitoh, Y. Li, and Y. Sugawara, *Study of oxidized* Cu(110) *surface using noncontact atomic force microscopy*, Surf. Sci. **602**, 2175 (2008).

[37] F. Cicoira, J. A. Miwa, M. Melucci, G. Barbarella, and F. Rosei, *Ordered assembly of α-Quinquethiophene on a copper oxide nanotemplate*, Small **2**, 1366 (2006).

[38] S. Berkebile, *Epitaxial organic films and their interfaces*, Ph.D. thesis; Karl-Franzes Universität Graz—Institute of Physics, 2009.

[39] F. Neese, *The ORCA program system*, WIRES Comput. Molec. Sci. **2**, 73 (2012).

[40] F. Neese, *Software update: the ORCA program system, version 5.0*, WIRES Comput. Molec. Sci. **12**, e1606 (2022).

[41] R. Krishnan, J. S. Binkley, R. Seeger, and J. A. Pople, *Self-consistent molecular orbital methods. XX. A basis set for correlated wave functions*, J. Chem. Phys. **72**, 650 (1980).

[42] A. McLean and G. Chandler, *Contracted Gaussian basis sets for molecular calculations. I. Second row atoms,* $Z = 11 - 18$, J. Chem. Phys. **72**, 5639 (1980).

[43] A. D. Becke, *Density-functional thermochemistry. III. The role of exact exchange*, J. Chem. Phys. **98**, 5648 (1993).

[44] P. J. Stephens, F. J. Devlin, C. F. Chabalowski, and M. J. Frisch, *Ab initio calculation of vibrational absorption and circular dichroism spectra using density functional force fields*, J. Phys. Chem. **98**, 11623 (1994).

[45] D. Jacquemin, I. Duchemin, and X. Blase, *Is the Bethe-Salpeter formalism accurate for excitation energies? Comparisons with TD-DFT, CASPT2, and EOM-CCSD*, J. Phys. Chem. Lett. **8**, 1524 (2017).

[46] M. Rohlfing and S. G. Louie, *Electron-hole excitations and optical spectra from first-principles*, Phys. Rev. B **62**, 4927 (2000).

[47] X. Blase, I. Duchemin, D. Jacquemin, and P.-F. Loos, *The Bethe-Salpeter equation formalism: From physics to chemistry*, J. Phys. Chem. Lett. **11**, 7371 (2020).

[48] P. Giannozzi *et al.*, *QUANTUM ESPRESSO: a modular and open-source software project for quantum simulations of materials*, J. Phys. Condens. Matter **21**, 395502 (2009).

[49] P. Giannozzi *et al.*, *Advanced capabilities for materials modelling with QUANTUM ESPRESSO*, J. Phys. Condens. Matter **29**, 465901 (2017).

[50] P. Giannozzi, O. Baseggio, P. Bonfà, D. Brunato, R. Car, I. Carnimeo, C. Cavazzoni, S. de Gironcoli, P. Delugas, F. Ferrari Ruffino, A. Ferretti, N. Marzari, I. Timrov, A. Urru, and S. Baroni, *QUANTUM ESPRESSO toward the exascale*, J. Chem. Phys. **152**, 154105 (2020).

[51] J. P. Perdew, K. Burke, and M. Ernzerhof, *Generalized gradient approximation made simple*, Phys. Rev. Lett. **77**, 3865 (1996).

[52] T. Sohier, M. Calandra, and F. Mauri, *Density functional perturbation theory for gated two-dimensional heterostructures: Theoretical developments and application to flexural phonons in graphene*, Phys. Rev. B **96**, 075448 (2017).

[53] M. S. Hybertsen and S. G. Louie, *Electron correlation in semiconductors and insulators: Band gaps and quasiparticle energies*, Phys. Rev. B **34**, 5390 (1986).

[54] J. Deslippe, G. Samsonidze, D. A. Strubbe, M. Jain, M. L. Cohen, and S. G. Louie, *BerkeleyGW: A massively parallel computer package for the calculation of the quasiparticle and optical properties of materials and nanostructures*, Comput. Phys. Commun. **183**, 1269 (2012).

[55] A. R. Altman, S. Kundu, and F. H. da Jornada, *Mixed stochastic-deterministic approach for many-body perturbation theory calculations*, Phys. Rev. Lett. **132**, 086401 (2024).

[56] F. H. da Jornada, D. Y. Qiu, and S. G. Louie, *Nonuniform sampling schemes of the Brillouin zone for many-electron perturbation-theory calculations in reduced dimensionality*, Phys. Rev. B **95**, 035109 (2017).

[57] S. Kaidisch, A. Kleiner, S. Refaely-Abramson, P. Puschnig, and C. S. Kern, *Photoemission tomography of excitons in 2D systems: momentum-space signatures of correlated electron-hole wave functions*, arXiv:2511.14956.

[58] M. Dauth, M. Wiessner, V. Feyer, A. Schöll, P. Puschnig, F. Reinert, and S. Kümmel, *Angle resolved photoemission from organic semiconductors: orbital imaging beyond the molecular orbital interpretation*, New J. Phys. **16**, 103005 (2014).

[59] G. H. Wannier, *The structure of electronic excitation levels in insulating crystals*, Phys. Rev. **52**, 191 (1937).

[60] Z. Tao, J. B. Habe, and J. B. Neaton, *Real-space quantification of exciton localization in acene crystals using Wannier function decomposition*, arXiv:2510.06539.